Solar Energy 202 (2020) 553–570

Contents lists available at ScienceDirect

Solar Energy

journal homepage: www.elsevier.com/locate/solener

Assessment of time resolution impact on the modeling of a hybrid CSP-PV plant: A case of study in Chile

Adriana Zurita[a,*], Carlos Mata-Torres[a], José M. Cardemil[b], Rodrigo A. Escobar[a,c]

[a] Departamento de Ingeniería Mecánica y Metalúrgica, Pontificia Universidad Católica de Chile, Vicuña Mackenna 4860, Santiago, Chile
[b] Departamento de Ingeniería Mecánica, Facultad de Ciencias Físicas y Matemáticas, Universidad de Chile, Beauchef 851, Santiago, Chile
[c] Centro de Energía, Centro del Desierto de Atacama, Escuela de Ingeniería, Pontificia Universidad Católica de Chile, Vicuña Mackenna 4860, Santiago, Chile

ARTICLE INFO

Keywords:
Chile
CSP-PV
CSP modeling
Hybrid plant
Time resolution

ABSTRACT

This study analyzes the time resolution impact on the modeling of a hybrid CSP-PV plant integrated with thermal storage and a battery bank for two locations in Chile. Daily and annual results were evaluated varying the time resolution from 1, 5, 10, 15, 30 to 60 min, as well as the capacity factor and LCOE. In this way, the CSP plant was the component most affected by the time resolution, followed by the battery dispatch, while the effect on PV production estimation was marginal. Control procedures of the receiver and power block were more realistically captured with time steps between 1 and 5 min, while with higher time steps, variability effects were neglected. Annual and techno-economic results indicate an overestimation of the total yearly production of the hybrid plant as the time step is increased, leading to an underestimation of the LCOE. Variations in the capacity factor and LCOE were around ± 2–3% in both locations using the 5-minute time step (with respect to the 1-min results), and between ± 4–6% using 10–60 min time steps. Different cases of study varying the dispatch strategy and components sizing were evaluated, showing that time resolution impact is lower for oversized PV configurations with respect to the CSP plant, and higher when the CSP plant is oversized with respect to the PV, regardless the dispatch strategy. Finally, this work provides some recommendations analyzing the advantages and drawbacks of implementing different time steps at each stage in the development of a hybrid solar power plant.

1. Introduction

Nowadays, Concentrated Solar Power (CSP) technology is proposed as an alternative to producie stable and continuous solar electricity with the integration of Thermal Energy Storage (TES). However, CSP technology has been less widely deployed than other renewable energy technologies such as solar Photovoltaics (PV) and wind, with only 5.5 GW of cumulative installed capacity around the world by the end of 2018 (REN21, 2019). In this way, CSP electricity costs are still superior to those of fossil fuel alternatives, even though its costs have been continuing to fall in the last years (IRENA, 2018). In contrast, PV costs have experienced substantial cost reductions driven by both declines in solar PV modules and balance of system costs, which have fallen solar PV costs to the fossil fuel costs range (IRENA, 2018), however, solar PV is still a variable generation mean that needs to be integrated with storage and flexibility options to guarantee the security of electric supply.

Following this, the concept of a hybrid CSP-PV plant has been widely studied by different authors in the last years to exploit the benefits of both CSP and PV technologies, showing that the hybrid scheme takes advantage of the low PV costs to achieve a lower Levelized Cost of Electricity (LCOE) and higher capacity factors than a same-sized CSP plant (Pan and Dinter, 2017). This concept was evaluated under the Atacama Desert conditions of Chile obtaining that is possible to achieve capacity factors higher than 85% with a hybrid CSP-PV plant and lower LCOEs than those of standalone CSP plants (Green et al., 2015; Starke et al., 2016, 2018; Bravo and Friedrich, 2018).

A hybrid CSP-PV plant, including a Battery Energy Storage System (BESS) at small scale, was studied by (Cocco et al., 2016; Petrollese and Cocco, 2016) analyzing different dispatch strategies of the hybrid system and evaluating the optimal configuration for two different locations in Morocco and Italy. Zurita et al. (2018) conducted a parametric study of a hybrid plant CSP-PV plant with a large-scale BESS obtaining a domain of solutions where the production of both CSP and PV plants with both types of storage can be integrated into a synergetic operation. Zhai et al. (2018) also optimized a hybrid CSP-PV plant to achieve the lowest LCOE, obtaining that a small battery improves the utilization time of the PV plant, while the CSP brings stability to the

* Corresponding author.
E-mail address: azurita1@uc.cl (A. Zurita).

https://doi.org/10.1016/j.solener.2020.03.100
Received 29 April 2019; Received in revised form 11 February 2020; Accepted 25 March 2020
Available online 16 April 2020

Nomenclature

Abbreviations

ACC	Air-Cooled Condenser
ACSP	CSP Association of Chile
BESS	Battery Energy Storage System
BoS	Balance of System
CD	Cerro Dominador
CF	Capacity Factor
CFWH	Closed Feed Water Heater
CSP	Concentrated Solar Power
DHI	Diffuse Horizontal Irradiance
DNI	Direct Normal Irradiance
EES	Equation Engineering Solver
EPC	Engineering, Procurement, and Control
GHI	Global Horizontal Irradiance
HTF	Heat Transfer Fluid
LCOE	Levelized Cost of Electricity
NRMSD	Normalized Root-Mean-Square Deviation
O&M	Operation & Maintenance
PCS	Power Conversion System
PPA	Power Purchase Agreement
PV	Photovoltaics
RSBR	Rotating Shadow Band Radiometer
SM	Solar Multiple
STEC	Solar Thermal Electric Components
TES	Thermal Energy Storage
TMY	Typical Meteorological Year
TRNSYS	Transient System Simulation
UA	Heat transfer coefficient

Symbols

A	area (m^2)
Af	capital recovery factor (-)
C	capacitance (kJ/K)/ total cost (USD)
c	specific cost (*)
Cap	capacity (%)
CF	capacity factor (%)
Cont	contingency percentage (%)
Cp	thermal capacity (kJ/kgK)
DNI	Direct Normal Irradiance (W/m^2)
E	annual electricity generation (MWh)
EPC	engineering and procurement cost percentage (%)
f	variation limit (W/m^2) / persistence (-)
Fa	availability factor (%)
h	height (m)
k	number of replacements of the BESS (-)
L	lifetime of the hybrid plant (yr)
LCOE	levelized cost of electricity (USD/MWh)
n	lifecycles of the BESS (-)
P	power (MW)
r	discount rate (%)
S	size in terms of energy (MWh)
SOC	state of charge (MWh) or (%)
T	temperature (°C/K)
t	replacement period of the BESS (yr)
W	power output (kW)
z	operating hours at maximum capacity per year of the BESS (h)
$\dot{m}$	mass flow rate (kg/s)
Δt	time step size (min)

(*) c can be given in USD/kW, USD/m^2, USD/MWh or USD/mSubscripts

amb	ambient
BESS	battery energy storage system
BoS	balance of system
c/d	charge or discharge
cap	capacitance
cond	condenser or turbine exhaust
CSP	concentrating solar power plant
d	direct
disch	discharged energy
DNI	direct normal irradiance
f	fixed
gross	gross
HF	heliostats field
HTF	heat transfer fluid
hybrid	hybrid plant
i	current time step
id	indirect
in	inlet
inst	installation labor
inv	investment
invs	inverter
lim	demand limit
min	minimum
mod	PV module
mode2	receiver control mode 2
net	net power
O&M	operation and maintenance
off	time delay to begin receiver start-up
other	other costs
out	outlet
overh	installer margin and overhed
pb	power block
PCS	power converion system
PV	photovoltaic plant
rec	receiver
rep	replacement
stor	storage section
t	time step size
TES	thermal energy storage
tow	tower
turb	turbine
v	variable
var	time for DNI variability

Superscripts

AC	AC size
DC	DC size
e	electric
n	normalized
th	thermal

power output.

More recently, Hamilton et al., (2019) developed a mixed-integer linear program to optimize the dispatch schedule of a CSP-PV plant with TES and a lithium-ion battery bank on a sub-hourly resolution to maximize the profits coming from electricity sales of the plant. The study considered the spot market in Chile and the utility market servicing northern and central California, and they compared results for both hybrid systems and a CSP-only system based on capacity factor,

LCOE, and Power Purchase Agreement (PPA). They also obtained that the hybrid plant radically outperforms the CSP-only plant from a techno-economic perspective.

In this way, literature has proven that the potential of a hybrid CSP-PV plant integrated with thermal and electric systems remains on the interaction between its components to supply a specific demand which would impact its dispatchability. Moreover, a PV system presents a more sensible response to the short-time variations of solar irradiance than a CSP-TES plant because the solar thermal power plants provide thermal inertia that allows smoothing transitory fluctuations. Nevertheless, except for the research done by (Cocco et al., 2016), most of the studies regarding the modeling of hybrid CSP-PV plants with storage have been performed using hourly time data.

This situation raises a question about what is the real impact that the time has on the production estimation of a hybrid power plant. Literature regarding the modeling of CSP plants suggests that a 10-minute time resolution would allow avoiding overestimations on the yield assessment of solar thermal power plants to achieve bankability, which could occur if only hourly time series are used (Hirsch et al., 2017). However, different temporal resolution has been used in the literature to analyze solar thermal power plants. For instance, Guédez et al. (2014) used a 10-minute time resolution to optimize a central-receiver system for peak power production. In a following study, Guédez et al. (2014a) considered an hourly time step to perform the optimization of a hybrid PV, wind, and CSP system with a gas burner as a back-up. Moreover, Guédez et al. (2016) used a 20-minutes time step to maximize the profit of a central receiver plant considering different operating strategies.

Meybodi and Beath (2016) conducted a systematic analysis with a multi-year solar database from Australia in which the time step of the simulation was varied from 5 to 60 min and the molten salt storage capacity from 4 to 12 h. Their results showed that smaller time steps such as 5 min could be used to obtain a realistic prediction of the CSP performance for optimizing purposes, while with the 60-minute data, it was obtained the lowest performance prediction and the least realistic. They also recommended time steps between 15 and 30 min to get an average representation of the real operation of the plant if computational time was a concern.

Regarding the time resolution of PV power plants, different authors have analyzed the effect of averaging the time-step. Ayala-Gilardón et al. (2018) analyzed the impact of time resolution on the self-consumption and self-sufficiency of different grid-connected PV systems using time steps ranging from 10 s to 1 year. They obtained that these values were overestimated with time steps larger than 1 h, concluding that using a low time resolution could cause the loss of relevant system information. Paravalos et al. (2014) also mentioned that the use of meteorological data with a 1-hour time step could result in a significant reduction of accuracy on the estimation of energy production of a PV plant.

In this manner, this paper presents a methodology to assess the impact of time resolution on the modeling of a hybrid CSP-PV plant with thermal and electric storage. The study considers a case study in Chile with two different locations that present different meteorological conditions. The performance of the hybrid plant was analyzed, varying both the time resolution of the solar data and the time step of the simulation from 1, 5, 10, 15, 30 to 60 min. Thus, this work allows understanding how the time resolution can affect the operation prediction of a hybrid plant, and the annual estimation of energy. This study also brings a new outlook about the influence of the solar variability on the dispatchability of the hybrid plant at a component level (PV, CSP-TES, and BESS), and how the temporal resolution influences the control procedures that rule the operation of the plant. Moreover, this work provides some recommendations to the different actors and phases involved in the development of a hybrid solar power plant, analyzing the advantages and drawbacks of implementing different time steps at every stage of the project.

Thus, Section 2 presents a description of the hybrid plant scheme; Section 3 describes the methodology to perform the modeling and simulations, and Section 4 explains the details of the techno-economic analysis. Results of this work are presented in three subsections: the daily plant performance for different day types was evaluated for both locations in Section 5.1, the annual performance analysis in terms of the total generation of each component of the plant is described in Section 5.2, and the influence of time resolution on the techno-economic evaluation for different cases of study is presented in Section 5.3. Finally, Section 6 presents the discussions, followed by the conclusions in Section 7.

2. System description

The hybrid plant model consists of a central receiver system and a PV power plant coupled to a direct molten salts TES and a lithium-ion

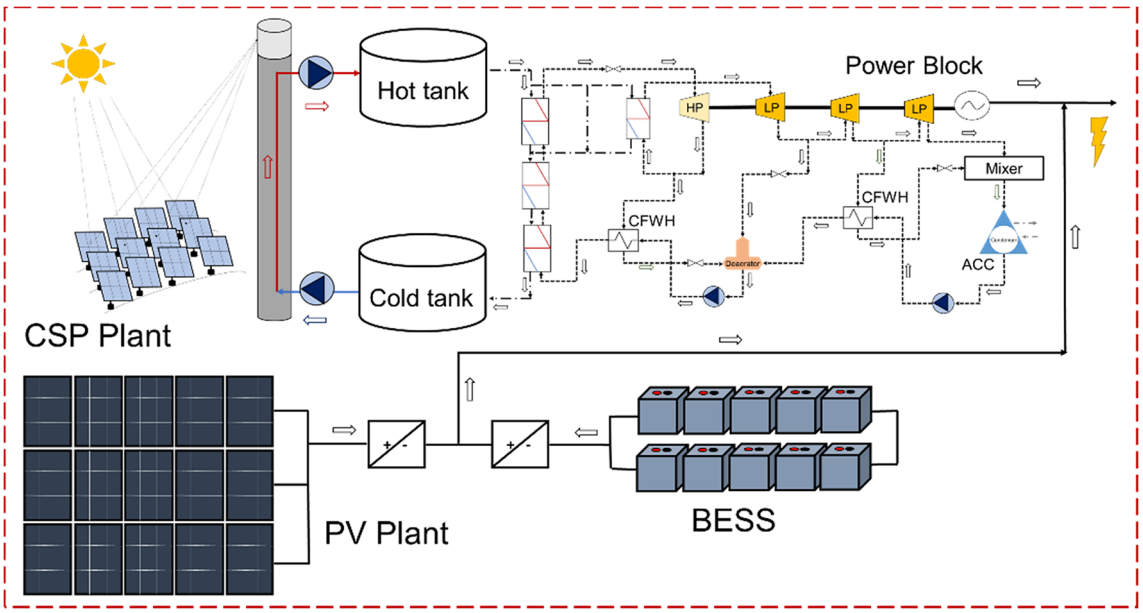

Fig. 1. Hybrid plant model scheme.

battery bank. Fig. 1 presents the complete scheme of the proposed hybrid plant. Each one of the plant components is described in this section.

2.1. CSP plant with TES and power block

The CSP plant is based on a molten salt central-receiver system technology that operates with a mixture of 60% $NaNO_3$ and 40% KNO_3. The TES section is a two-tank direct system where the molten salts work as Heat Transfer Fluid (HTF) and storage media. The cold and hot tank temperatures are set at 295 °C and 565 °C. The heliostats field configuration and efficiency, the receiver height, receiver diameter, and tower height are optimized in terms of the Solar Multiple (SM), which represents the ratio between the thermal power output produced by the solar field at design conditions and the heat required by power cycle at the nominal point.

The power block of the CSP plant consists of a Rankine cycle with a nominal efficiency of 39.12% and a gross power output of 110 MW_e. The power block is composed by a steam train generator which includes a reheating stage, two Closed Feed-Water Heaters (CFWH), a deaerator, two feed-water pumps, an Air-Cooled Condenser (ACC), and a turbine with a high-pressure stage and three mass flow rate extractions in the low-pressure stages. The maximum power cycle temperature is limited to 550 °C, and the minimum turbine load is 30% of the gross power. Table 1 presents the main design parameters of the CSP plant and power block.

2.2. PV plant and BESS

The PV plant consists of a fixed-angle module configuration. The solar cell technology considered was silicon mono-crystalline based on the MEMC-330 Sun Edison modules (SunEdison, 2015) with a nominal power of 330 W_{dc}. The inverter is an ULTRA-TL-1100 of ABB with a maximum AC power of 1 MW_{ac} (ABB, 2017). The PV plant has a scalable size in terms of the number of inverters to reach the nominal PV capacity. A fixed soiling rate of 0.5% per day was also considered (Zurita et al., 2018).

The BESS section is a lithium-ion battery bank with a maximum discharge depth of 84%. The BESS couples to a Power Conversion System (PCS) with a power rating of 100 MW. Table 2 presents the main design parameters of the PV plant and BESS.

3. Modeling and simulation

The hybrid plant was modeled with the Transient System Simulation Program (TRNSYS) to obtain the annual performance and operation curves of the thermal and electric systems of the plant under transient conditions. Simulations were performed throughout a year varying the time step from 1, 5, 10, 15, 30 to 60 min. The model was developed in a single TRNSYS deck to evaluate the interactions between all the plant components. Ground-measurements of solar irradiation with a 1-minute time resolution were implemented to create a new set of data files, averaging the 1-minute gross data for each time step. The following subsections will explain the solar database features, the simulation models, and the plant operating modes.

3.1. Location and solar resource

The study considered two different locations in Chile: Carrera Pinto and Santiago of Chile. Fig. 2 shows the Direct Normal Irradiance (DNI) measured during 2015 and 2013 for Carrera Pinto and Santiago, respectively. Both locations were chosen since they present different weather features. Carrera Pinto is in a vast desert plain where extremely arid conditions are predominant throughout the year. This location shares the high radiation levels and features that are typical in northern Chile, with low aerosol content, a minimum cloud cover, and high clear-sky indexes in many days throughout the year.

In contrast, Santiago is the capital city of Chile located next to the Andes high range in the central region with a relatively dry climate, heavy aerosols, and pollution episodes during winter. Solar resource in Santiago presents a high variability throughout the year with a strong seasonality due to a typical presence of persistent cloud covers during winter (Escobar et al., 2015). This location represents a place of relevance in terms of energy demand for the country, as it is representative of the meteorological conditions in the central region of Chile.

Meteorological and solar data comes from ground station measurements situated in Carrera Pinto and Santiago. Table 3 presents the main features of both ground stations. Carrera Pinto's station is in the site where it is planned to be deployed the Copiapó project in the Atacama Region of Chile, while Santiago's station is at Pontificia Universidad Católica de Chile. Both stations operate under the Baseline Surface Radiation Network standards and guidelines, and their main features and instruments are accurately described by Escobar et al. (2015) and Rojas et al. (2019).

The gross data coming from both ground stations was obtained with a 1-minute time resolution. Quality criteria used to evaluate the data is described by (Rojas et al., 2019). Then, only valid data was considered to create a new set of data files averaging the 1-minute data for each one of the time steps (5, 10, 15, 30, and 60 min).

3.2. PV plant and battery bank model

The PV plant was simulated as an array with a scalable size in terms of the number of inverters, considering a maximum inverter power output of 1 MW_{ac}. The model was implemented using the Type 190 of TRNSYS, which allows to include the inverter efficiency curve as an input. The validation of the PV plant model has been presented in previous studies (Valenzuela et al., 2017; Zurita et al., 2018). The BESS model is based on Eq. (1) that describes the variation of State of Charge (SOC) on the battery bank given a charge or discharge rate ($\eta_{c/d}$) from a previous time step *(i-1)* to the next *(i)*,

Table 1
Main design parameters of the CSP plant and the power block under nominal conditions.

Description	Unit	Value
CSP plant		
CSP technology	–	Central receiver
Design receiver temperature	°C	565
Heliostat area	m^2	144
Reflectivity of the heliostat field	%	95
TES system	–	Two-tanks direct
HTF and storage media	–	Molten salts mixture
Power block		
Gross power output	MW	110
Net output of electricity	MW	100
Minimum operation condition	%	30
Nominal thermal efficiency	%	39.12
Design ambient temperature	°C	30
Design steam mass flow rate	kg/s	630
Design HTF fluid inlet temperature	°C	565
Design HTF fluid outlet temperature	°C	295
Inlet of the high-pressure turbine	bar	100
Inlet of the medium-pressure turbine	bar	22
Inlet of the low-pressure turbine	bar	10
Condensing pressure	bar	0.012
Superheater pinch point	°C	15
Evaporator pinch point	°C	30
Reheater pinch point	°C	20
CFWH terminal temperature difference	°C	5
High-pressure turbine efficiency	%	90
Medium and low-pressure turbine efficiency	%	86
Condensate pumps efficiency	%	80
Generator efficiency	%	96

Table 2
Main parameters of the PV plant and BESS.

Description	Unit	Value
PV Plant		
Solar Cells Technology	–	m-cSi
Inverter Power	kW_{ac}	1000
Inverter Efficiency	%	98.4
Module Area	m^2	1.956
Module Power	W	330
Module Efficiency	%	16.9
BESS		
Depth of Discharge	%	84
Overall Efficiency	%	94
Life Cycles	cycles	5000
Calendar Life	yr	20

$$SOC_{(i)} = SOC_{(i-1)} + \eta_{c/d} \cdot P_{BESS} \cdot 1/60 \cdot \Delta t \quad (1)$$

where P_{BESS} is the charge or discharge power of the battery, and Δt is the simulation time step in minutes. The type developed for the battery is also described in detail by (Zurita et al., 2018).

3.3. Power block model

The power block model was developed in the Equation Engineering Solver (EES) based on previous works (Mata-Torres et al., 2019) to obtain the performance under nominal and off-design conditions. The model is comprised of mass, energy, and heat transfer balances at every component of the Rankine Cycle illustrated in Fig. 1. The design conditions consider the parameters presented in Table 1 to calculate the design overall heat transfer coefficients (UA) of heat exchangers, the design HTF mass flow rate, and the thermal design efficiency of the cycle. The off-design model considers a constant pressure control for the part-load operation, and it calculates the heat-exchangers effective UA under variations of the steam mass flow rate based on the equations described by Patnode (2006). Variations in efficiency and pressures of the steam turbine were also considered according to the Stodola's ellipse law.

The EES model was used to create a performance map of the power block through a parametric analysis varying three operational conditions: the inlet hot HTF temperature (T_{inHTF}), the HTF mass flow rate ($\dot{m}_{inHTF}$), and the ambient temperature (T_{amb}), considering 6048 points for a valid range described in Table 4.

Then, a polynomial multi-variable regression model was developed, employing the data coming from the parametric analysis. Output variables of the regression model were: the net power output from the turbine-generator (W_{net}), the exhaust mass flow rate of the turbine ($\dot{m}_{cond}$) and temperature of the HTF returning to the solar field (T_{outHTF}). The equations and coefficients of the multi-variable polynomial regression model are provided in detail in Appendix A. Supplementary Data.

Table 3
Meteorological station features.

Description	Carrera Pinto	Santiago
Latitude (°)	27.083 S	33.497 S
Longitude (°)	69.93 W	70.61 W
Altitude (m)	1640	580
Ground station type	RSBR	Sun tracker
Yearly total of DNI (kWh/m^2-yr)	3462.58	2153.78
Yearly total of GHI (kWh/m^2-yr)	2519,47	1941.07

Table 4
Applicable range of the power block polynomial regression.

Variable	Units	Applicable range
T_{inHTF}	°C	[500:565]
$\dot{m}_{inHTF}$	kg/s	[160:630]
T_{amb}	°C	[0:40]

The polynomial regressions were used to create a new component in TRNSYS that allows evaluating the power block operation in a significantly lower computational time. The Normalized Root-Mean-Square Deviation (NRMSD) was utilized to assess the errors associated with the regressions, achieving NRMSDs of 0.13%, 0.01% and 0.80%, corresponding to the W_{net}, $\dot{m}_{cond}$, and T_{outHTF}, respectively.

3.4. Central receiver power plant model

The central-receiver plant model was developed using different components developed by authors and existing components of TRNSYS libraries. The heliostats field was modeled using a component based on Type 394 of the Solar Thermal Electric Components (STEC) library (Schwarzbözl et al., 2006), which provides the incident power on the receiver surface, including a daily soling rate and cleaning period (Zurita et al., 2018). This type uses as input a matrix indicating the field efficiency at different solar azimuth and zenith angles, which interpolates during the simulation to obtain the heliostats field efficiency in terms of solar position. Moreover, the TES system was modeled

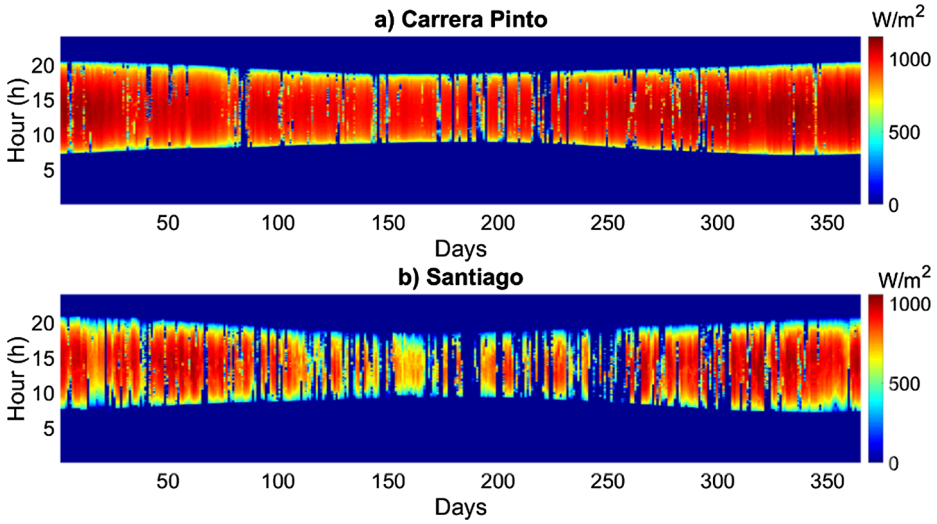

Fig. 2. DNI profile in a) Carrera Pinto and b) Santiago.

considering two tanks (hot and cold tank) with variable volume, using the Type 39 from TRNSYS library, in which the HTF pump consumption by the power block was also considered.

Regarding the central receiver, a new component was also developed by authors that include the modeling of a cylindrical tubular central receiver. The developed model calculates in a simplified manner the thermal power absorbed by the HTF in the receiver based on the work developed by (Wagner, 2008), introducing as inputs the receiver and tower dimensions, which are optimized in terms of the SM using SolarPILOT from the (National Renewable Energy Laboratory (NREL), 2018). The model formulation considers an equations system of energy balances on a receiver tube element, including the incident radiation and thermal losses, which are constituted by radiation, natural and forced convection losses. Thus, the outlet HTF mass flow rate and temperature are calculated in terms of the absorbed thermal power, while the receiver surface temperature is calculated considering the heat transfer across the receiver tube wall from the HTF fluid running through the tube to the receiver surface. Since there are many relationships in the equation system, the receiver model comprises an iterative process that is computed until the receiver surface temperature, the HTF outlet temperature, and the HTF mass flow rate in the receiver converge. The electric power consumption of the HTF tower pumps is also considered.

Besides, the receiver includes the simple modeling of a thermal capacitance to represent the thermal inertia of the receiver. With this purpose, an adiabatic capacitance was added after the receiver calculation, in which the inlet stream is the HTF outlet mass flow rate of the receiver, and the outlet stream is the HTF mass flow rate that goes to the hot TES tank with the capacitance temperature. The performance of the thermal capacitance is assessed by following the next differential equation:

$$C^{th}\frac{dT_{cap}}{dt} = \dot{m}_{HTF}\,Cp\,T_{rec,out} - \dot{m}_{HTF}\,Cp\,T_{cap} \tag{2}$$

where C^{th} is the thermal capacitance in kJ/K, $T_{rec,out}$ is the HTF outlet temperature of the receiver in K, T_{cap} is the capacitance temperature in K, $\dot{m}_{HTF}$ is the HTF mass flow rate in kg/s, and Cp is the heat capacity of the HTF in kJ/kg-K. This approach allows adding the thermal inertia to the receiver performance without penalizing the computational time. A more detailed approach could be considered if the thermal inertial term is introduced in the energy balance of the receiver tube and the HTF fluid. However, the iterative process would be more complex, and it would require a significantly higher computational time to converge. Moreover, the thermal inertia was considered only for the time steps under 30 min, due to its effect is not representative for low time resolution.

3.4.1. Control modes of the central receiver operation

The operation of the central receiver is one of the most critical points at the time of simulating a solar tower power plant. Due to the fluctuating nature of solar radiation, solar tower power plants are exposed to transient effects; however, the thermal power generation does not follow the fluctuating irradiance instantaneously since there are large amounts of molten salts and pipes providing thermal inertia to the system. Despite this, information regarding operation controls of molten salts central receiver systems is difficult to obtain since there are very few of them successfully operating around the world, and the access to this information is limited.

This study evaluates the performance of the central receiver with sub-hourly simulations, which makes necessary to implement control procedures that capture the effects of DNI variability. Following this, a set of control parameters were applied to attempt simulating the most similar performance to that observed in CSP operating facilities. In this way, assumptions made in this study are based on the experience provided by some experts in CSP plants; and the Engineering, Procurement, and Control (EPC) of current CSP projects.

In first instance, the operation considers the limitations of starting up the receiver through three control parameters:

1. A minimum energy level required to start-up, set at 25% of the energy produced by the receiver at the design point for one hour.
2. A minimum thermal power required to begin the start-up procedure, set at 20% of the receiver design thermal power.
3. A minimum thermal power to start the effective operation of the receiver, set at 25% of the receiver design thermal power.

Furthermore, two control modes to operate the receiver were established to regulate the mass flow rate and the outlet HTF temperature in the receiver:

1. A perfect mass flow rate control (mode 1): in this control mode, the HTF mass flow rate in the receiver is calculated to maintain constant the HTF design outlet temperature at the receiver. This mode is commonly activated in stable periods of DNI, such as during clear-sky days or periods with low variability.
2. A fixed mass flow rate control (mode 2): in this control mode, the HTF outlet temperature is calculated to maintain a constant HTF mass flow rate in the receiver, allowing the HTF outlet temperature to vary within a safety limit during variable conditions of DNI. This mode is activated during intermittent cloudy days or periods with a high DNI variability, ensuring the receiver integrity. In this case, if the receiver outlet temperature falls below 470 °C, the HTF flow is diverted to the cold tank to avoid excessive cooling in the hot tank. Moreover, the fixed mass flow rate is computed as 105% of the maximum flow calculated by the mode 1 in the last 30 min.

Following this, a maximum DNI variation limit (f_{DNI}) was defined that must be surpassed to change from mode 1 to mode 2. This limit was set at 10 W/m^2/min, and it was chosen evaluating the natural variability of the DNI during a clear-sky day to ensure not obtaining misleading results. The DNI variability ($f_{DNI\,(i)}$) was calculated with the persistence of the DNI, as the following equation indicates:

$$f_{DNI\,(i)} = \frac{|DNI_{(i)} - DNI_{(i-1)}|}{\Delta t}\left[\frac{\frac{W}{m^2}}{min}\right] \tag{3}$$

where $DNI_{(i)}$ is the DNI at the current time step, $DNI_{(i-1)}$ is the DNI at the previous time step, and Δt is the time step in minutes. Besides, it was implemented four time-delay parameters in terms of the variability to control how much time every mode would be activated and to establish start-up delays:

1. $t_{\text{min\_mode2}}$: it is the minimum amount of time in which the receiver must operate at mode 2 when it changes from mode 1. It was set at 60 min.
2. $t_{\text{var\_mode2}}$: it is the minimum amount of time in which the DNI variability must not exceed the f_{DNI} for the receiver to be able to change from mode 2 to mode 1. If the DNI variability exceeds the f_{DNI}, the time delay is reset, and the receiver continues operating at mode 2. It was set at 15 min. This parameter ensures that the variability conditions of DNI must be under a limit to return to mode 1.
3. $t_{\text{off\_1}}$: it is the time delay to begin the start-up procedure of the receiver. This time delay is only activated if the receiver was previously turned-off and it is reset if DNI variability exceeds 100 W/m^2/min (10 times f_{DNI}) within this time. It was set to 120 min. This parameter ensures that the receiver will not begin the start-up procedure during highly variable days.
4. $t_{\text{off\_2}}$: it is a second-time delay to begin the startup procedure, in which the DNI variability must not exceed 20 W/m^2/min (2 times f_{DNI}). If the DNI variability exceeds this threshold while the receiver is off, the time delay is reset, and the receiver will not initiate the

startup. It was set at 15 min. This parameter ensures that the variability conditions of DNI must be under a limit to begin the start-up procedure. In this way, both t_{off_1} and t_{off_2} must have been fulfilled to begin the start-up.

For a better understanding of these parameters, Fig. 3 illustrates the operation of the central receiver for two days with a clear-sky and a variable DNI profile in Carrera Pinto using a 1-minute time resolution. In this case, the central receiver has a design thermal power of 512 MWt corresponding to a 100 MW CSP plant with a SM of 2 and 14 h of TES. Fig. 3 shows the incident power coming on the receiver, the start-up power, and the effective receiver for a clear-sky and a variable day. The control mode leading the receiver operation is also shown down in the graphs.

At the beginning of the clear-sky day (Fig. 3a), the receiver takes between 30 and 40 min in the start-up process before initiating its effective operation. It is observed that the receiver starts operation at mode 2, but it changes to mode 1 in a few minutes, maintaining this mode for the rest of the day. Approximately at 15:00 h, the hot tank reaches its maximum level of molten salts, which causes a defocusing of the heliostats to remain stable the hot tank volume. Three hours later, the CSP plant starts to operate since the PV output starts decreasing. It is observed that the receiver does not require a start-up procedure to begin operation again since it is supposed that a small part of the heliostats remain focused to keep warm the receiver while the hot tank is full. Finally, Fig. 3a also shows that the HTF outlet temperature in the receiver remains stable in the design point throughout the day due to control mode 1.

In contrast, Fig. 3b shows a day with a variable DNI profile presenting values close to 100 W/m^2 in some moments of the day. During the first hours of the day, the receiver delays the start-up procedure due to DNI variability, but it starts regular operation after reaching the minimum energy required. The receiver operates in mode 1 approximately until 13:00 h, when it switches to the mode 2, due to a DNI variability event. During this period, it is observed a variation in the HTF outlet temperature between 510 and 565 °C, which leads to a temperature decrease in the hot TES tank. After the 14:30 h, the receiver is turned off because the incident power is lower than the minimum thermal power to operate. In this way, the receiver is not restarted in the rest of the day due to the startup delay times are activated. It is also worth to mention that before the receiver is shut down, the thermal inertia allowed to keep working the receiver for around five more minutes.

3.5. Operating mode

The operating mode of the hybrid plant considers delivering a base demand (P_{lim}), which was defined at 100 MW$_e$ for the base case of this study. In this way, the PV output has priority to cover the demand, while the CSP plant operates as a back-up of the PV output, and the BESS is activated when the CSP-PV production is not enough to cover the demand. Fig. 4 shows a flow chart describing the operation mode of the hybrid plant, where P_{pb} is the power block nominal output, $P_{PV\,(i)}$ is the PV net output (subtracting the parasitic consumption of the heliostats and the tower), $P_{CSP\,(i)}$ is the CSP power output, $P_{PV,exc\,(i)}$ is the PV surplus that charges the batteries or that becomes in dumped energy, $P_{BESS\,(i)}$ is the battery output power, $SOC_{(i)}$ is the batteries' SOC and Cap_{min} is the minimum capacity of the batteries.

In this manner, when the PV output is $0.4P_{pb}$ below P_{lim}, the PV + CSP plant operates together to cover the demand. When the PV production is $0.4P_{pb}$ above P_{lim}, but it is not enough to fulfill the demand, the CSP plant operates at minimum power block condition ($0.3P_{pb}$) while the PV surplus is stored in the BESS or dumped if the BESS is completely charged. If the PV output is at least $0.1P_{pb}$ below P_{lim}or higher than the baseload capacity, the power block of the CSP plant is turned off, and the PV surplus is used to charge the BESS, or it is dumped if the BESS is completely charged. In this case, if the receiver is also operating because there is enough incident power coming from the solar field, then the TES is charged, but if the TES reaches its maximum level, the heliostats are defocused, and there is a solar field dumped energy.

In contrast, the BESS discharge is only activated when the PV-CSP output is below 2 MW of the P_{lim}. This can occur during high-frequency DNI transients that cannot be fulfilled by the CSP plant, during the

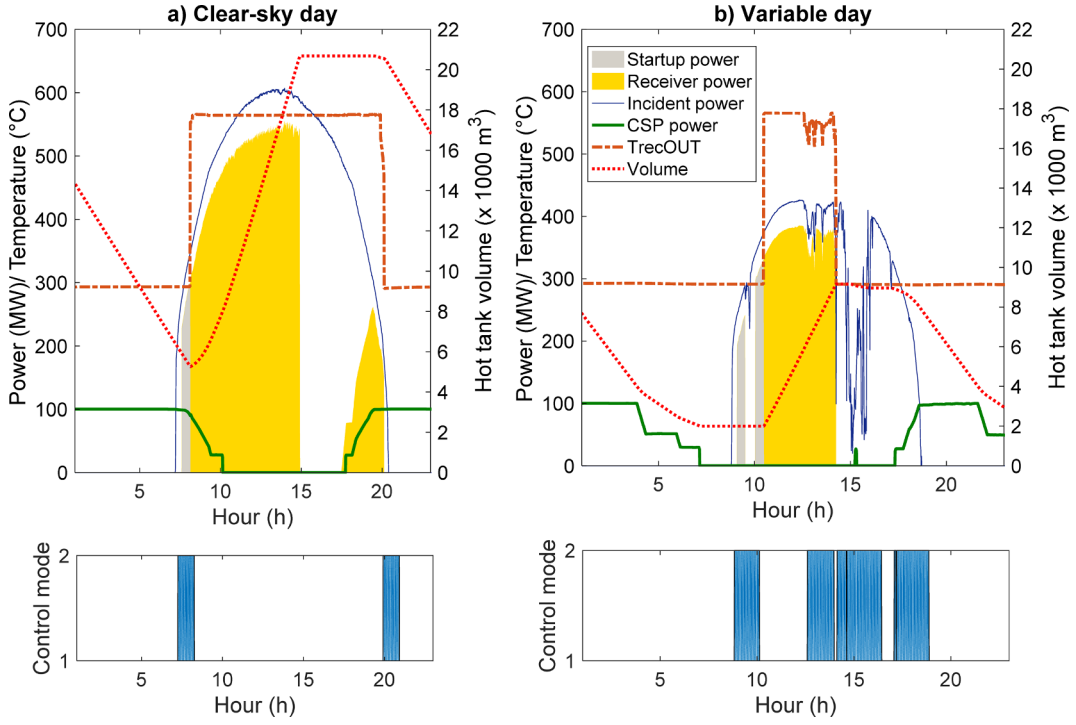

Fig. 3. Receiver operation in Carrera Pinto with 1-minute time resolution for two types of days: a) Clear-sky day, and b) Variable day.

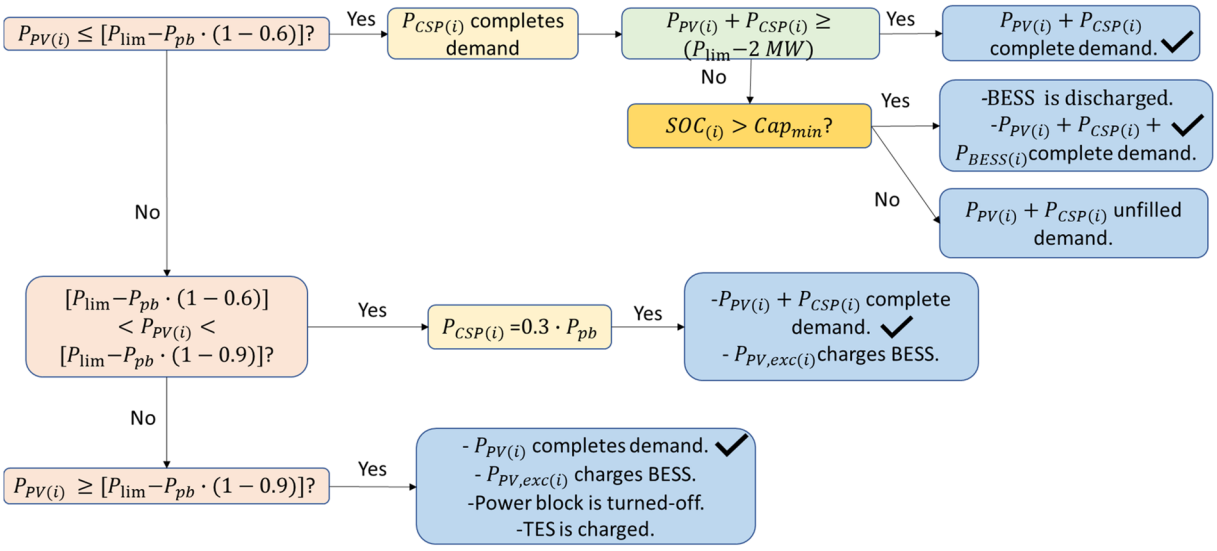

Fig. 4. Operating mode of the hybrid plant.

start-up and shutdown procedures of the CSP plant (limited by the ramps load of the power block), and when the TES is running out of energy.

Controllers of the TES system and power block were applied in TRNSYS, monitoring the volume that can be charged and discharged in the hot tank. Different procedures to operate the start-up and shutdown of the plant were also implemented to increase or decrease the power output of the Rankine cycle. Hot and cold start-up and shut down procedures of the power block are explained in detail in a previous work performed by the authors (Zurita et al., 2018).

4. Techno-economic analysis

The economic analysis was based on the computation of the LCOE for the hybrid plant based on the definition of (IRENA, 2012) and represented by Eq. (4),

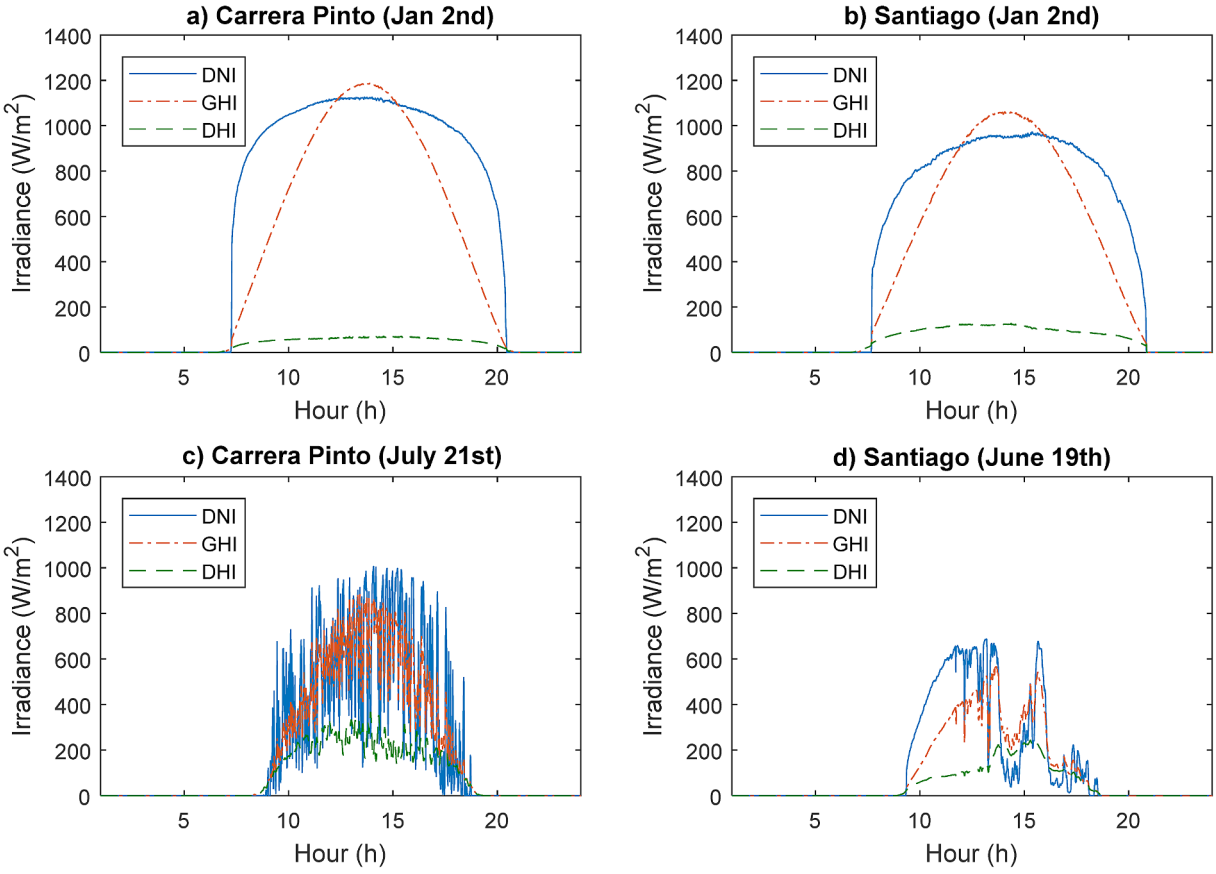

Fig. 5. Solar irradiance in a 1-minute time scale for a) a clear-sky day in Carrera Pinto, b) a clear-sky day in Santiago, c) a variable day with high-DNI levels and high-frequency transients in Carrera Pinto and, d) a variable day with low DNI levels in Santiago.

$$LCOE = \frac{Af \bullet (C_{inv,hybrid} + C_{rep,BESS}) + C_{O\&M,hybrid}}{E_{hybrid} \bullet Fa} \quad (4)$$

where Af is the capital recovery factor; $C_{inv,hybrid}$ is the total investment cost of the hybrid plant including the PV ($C_{inv,PV}$), CSP ($C_{inv,CSP}$), and BESS investment costs ($C_{inv,BESS}$); $C_{rep,BESS}$ is the replacement cost of the battery bank throughout the lifetime of the hybrid plant; $C_{O\&M,hybrid}$ is the total operation and maintenance (O&M) cost of the hybrid plant; E_{hybrid} is the annual electricity generation of the hybrid plant and Fa is the availability factor defined in 95%. The project lifetime considered was of 35 years with a discount rate of 5% which is in concordance with the prices offered by the CSP projects in Chile. The capacity factor (CF) was also computed as a technical indicator of the hybrid plant, and it is calculated as Eq. (5) indicates:

$$CF = \frac{E_{hybrid}}{P_{lim} * 8760h} \bullet Fa \quad (5)$$

CSP investment costs are comprised of direct and indirect capital costs representing those expenses applied in the year zero of the project, while the O&M costs represent the annual expenditures that occurred after the system is installed. The CSP cost database implemented for this study is in concordance with the values reported by the CSP Association of Chile (ACSP) in 2019, which represent costs reported in the literature for central-receiver plants (Jorgenson et al., 2016; Dieckmann et al., 2017; Kassem et al., 2017; Sharma et al., 2017; Boretti, 2018; Aly et al., 2019) validated by the industry in Chile. This economic data is presented in detail in Appendix B. Cost Data.

In the case of the PV plant, the module cost is based on the spot prices reported by PV Info Link (2018), while the inverter, balance of system (BoS), and the rest of the costs are based on the values reported by NREL for utility-scale PV plants in 2018 (Fu et al., 2018a). BESS costs are based on the values reported by NREL (Fu et al., 2018b) for PV-BESS plants with a lithium-ion battery bank of 2-hour duration. It was also considered the lifecycle method implemented by Zakeri and Syri (2015), which examines the total capital cost of an electric energy storage unit and the lifecycle costs related to the O&M and replacement. In this way, equations and cost data implemented to perform the economic analysis are presented in detail in Appendix B. Cost Data and Appendix C. Cost Structure.

5. Results

This study considered different time steps ranging from 1, 5, 10, 15, 30 to 60 min to evaluate the DNI variability effects on the dispatchability of the hybrid plant and the receiver operation. In the analysis, the simulation time step was equaled to the solar data time resolution. Therefore, the input of total solar irradiation was the same for each time step evaluated.

5.1. Daily operation curves

A base case scenario with a hybrid plant configuration of 190 MW of nominal PV size, a SM of 2, 14 h of TES and 400 MWh was chosen to analyze its performance under different operational conditions. This configuration was based on the results obtained by (Zurita et al., 2018) for a hybrid plant with 400 MWh of BESS. Simulations were conducted in both Carrera Pinto and Santiago.

Three types of day were chosen to compare the operation of the hybrid plant. Fig. 5 shows the three components of the solar irradiance for a clear-sky day (January 2nd) in both locations, a variable day with high levels of DNI and high-frequency transients (July 21st) in Carrera Pinto, and a variable low-level DNI day (June 19th) in Santiago, showing the Global Horizontal Irradiance (GHI) and the Diffuse Horizontal Irradiance (DHI). Fig. 5a and Fig. 5b illustrate a clear-sky day with a typical profile of solar irradiation and high levels of DNI, with a maximum DNI of 1127 W/m^2 and 972 W/m^2 in Carrera Pinto and Santiago, respectively. In contrast, Fig. 5c shows the solar irradiance in Carrera Pinto for a day with high-frequency transients and DNI values between 400 and 1000 W/m^2. A variable day with lower DNI levels and less variability is also presented in Fig. 5d showing a more consistent cloudy condition throughout the day, reaching a maximum DNI of 688 W/m^2 and values below 100 W/m^2 during some hours in the mid-afternoon.

Daily total generation of the hybrid plant for the clear-sky day (January 2nd) in both Carrera Pinto and Santiago is presented in Table 5 using different time steps. This table shows the daily total maximum PV energy (without considering the curtailment of the baseload demand and the parasitic consumptions of the hybrid plant), the CSP and BESS plant total generation, and the total daily energy generated by the receiver.

In both locations, it is observed that the prediction of the daily production of all the components barely present variations as the time step is increased, (below 1%) since the irradiance profile is quite stable throughout this day. Moreover, differences in the daily hybrid total generation were below ± 0.03% as the time step was increased in both locations with respect to the 1-minute results, indicating that the influence of time resolution on the operation prediction is negligible during a clear-sky day.

In contrast, Table 6 shows the daily total generation results for two different types of variable day, one with a highly variable irradiance profile on July 21st in Carrera Pinto, and another more consistent cloudy condition with a lower degree of variability on June 19th in Santiago. In Carrera Pinto, differences in the daily net PV output are still below 1% as the time step is increased (with respect to the results obtained with the 1-minute data); nevertheless, the most remarkable variations were obtained in the CSP plant operation. Results show that the receiver does not start operation when the simulation is performed with the 1-minute time resolution, and the CSP plant does not provide energy during this day. Same situation occurs when a 5-minute time resolution is considered (with the only difference of some hours in which the hot tank is discharged in the early morning which accounts for the 456 MWh of CSP production), while from 10 to 60 min of time step, the production prediction significantly changes since the receiver does operate. These results are illustrated in Fig. 6, which shows that the variability of the PV output is reduced dramatically as the time step is increased, leading to discharge the BESS at later hours.

The cause behind the variation of the CSP plant can be elucidated in

Table 5
Daily total generation using different time steps for a clear-sky day (Jan 2nd) in Carrera Pinto and Santiago.

	January 2nd in Carrera Pinto (MWh/day)					January 2nd in Santiago (MWh/day)				
Time step (min)	PVmax	CSP	BESS	Hybrid	Receiver	PVmax	CSP	BESS	Hybrid	Receiver
1	1,291.97	1,472.05	9.00	2,400.59	3,749.24	1,151.65	1,459.06	33.63	2,399.78	3,848.46
5	1,292.77	1,471.75	7.66	2,400.69	3,757.80	1,154.23	1,458.69	32.59	2,399.87	3,841.26
10	1,292.58	1,476.90	5.58	2,401.17	3,735.13	1,155.64	1,461.87	30.01	2,399.40	3,832.00
15	1,292.23	1,478.29	4.56	2,400.83	3,771.05	1,156.14	1,461.94	30.75	2,400.00	3,860.59
30	1,290.30	1,489.23	3.24	2,401.25	3,795.42	1,157.17	1,475.90	25.68	2,400.00	3,815.11
60	1,285.04	1,489.78	8.35	2,401.22	3,805.43	1,157.56	1,457.98	32.18	2,400.00	3,852.39

Table 6
Daily total generation using different time steps for a day with high-frequency transients of DNI (July 21st) in Carrera Pinto and a cloudy day (June 19th) in Santiago.

	July 21th in Carrera Pinto (MWh/day)					June 19th in Santiago (MWh/day)				
Time step (min)	PVmax	CSP	BESS	Hybrid	Receiver	PVmax	CSP	BESS	Hybrid	Receiver
1	954.34	0.00	190.62	944.64	0.00	625.33	9.40	39.44	630.95	182.27
5	960.61	456.60	409.94	1,634.58	0.00	625.44	43.43	38.33	664.43	399.60
10	962.80	839.48	428.09	2,031.55	941.87	625.87	88.42	35.25	708.74	586.60
15	963.44	936.08	425.45	2,130.32	1,162.04	624.92	133.35	35.45	751.16	471.86
30	964.13	849.72	429.66	2,050.85	1,087.16	622.60	120.45	32.16	737.41	300.66
60	957.48	864.32	430.40	2,063.17	1,359.26	602.52	174.70	22.69	770.39	581.45

Fig. 7, which illustrates the receiver and TES operation for July 21st in Carrera Pinto. This figure shows that in the 1-minute simulation, the receiver does not start operation due to minimum conditions established by controls to start-up are not achieved throughout the whole day. This is mainly due to the continuous intermittency of the DNI profile and because the minimum energy required to begin operation is not reached. Moreover, the hot tank is not charged or discharged since, at the beginning of the day, it is at its minimum level, and the receiver does not operate to heat the molten salts during the day.

In contrast, as the time step is increased, the DNI variability is significantly reduced since the solar irradiance is averaged at every-time step. Therefore, it is observed that simulations using 10 to 60-minutes time resolution predict less variable conditions of DNI, which favor the conditions to starting up the receiver approximately before mid-day. Under these conditions, the receiver operates for most of the day, charging the hot tank and fulfilling the demand during the night. These differences in the operation have a high impact on the daily prediction of the hybrid plant generation due to the variations on the CSP performance. In this way, it was obtained that the production of the hybrid plant with the time step of 10 min is more than double the predicted energy using the 1-minute time resolution. Moreover, when time steps between 15 and 60 min are implemented, differences in the hybrid generation prediction are within a range between 1 and 5% with respect to the 10-minute time resolution results.

In the case of Santiago, results for a variable day with lower values of DNI indicate that differences in the PV generation as the time step increase are marginal, while the most significant variations occurred in the receiver and CSP plant production. As Fig. 8 shows, the receiver presents a different performance as the time step is varied. As it happened with the intermittent day in Carrera Pinto, the DNI variability is significantly reduced as the time resolution is decreased, however, since there are periods with very low values of irradiance in the afternoon, the receiver effectively operates less time in comparison to the other day. It is observed that with the 1-minute time resolution, the conditions to start the operation of the receiver are initially reached in the morning. However, since it is followed by a period of low DNI, the receiver only operates for a few hours. This operation tendency remains as the time step is increased, varying only the number of hours that the receiver operates. Therefore, the daily prediction of CSP production tends to grow with the time step. It is also worth to mention that if a perfect forecasting of the DNI was integrated into the simulation, the receiver might not operate at least under the conditions of the 1-minute time resolution since the receiver operation time is very small.

In this way, overall results regarding the daily performance of the hybrid plant indicate that the performance of thermal systems such as the receiver and the power block of the CSP plant was the most affected by the time resolution. These variations in the time step of the simulation had an impact on the operation controls of these systems, such as

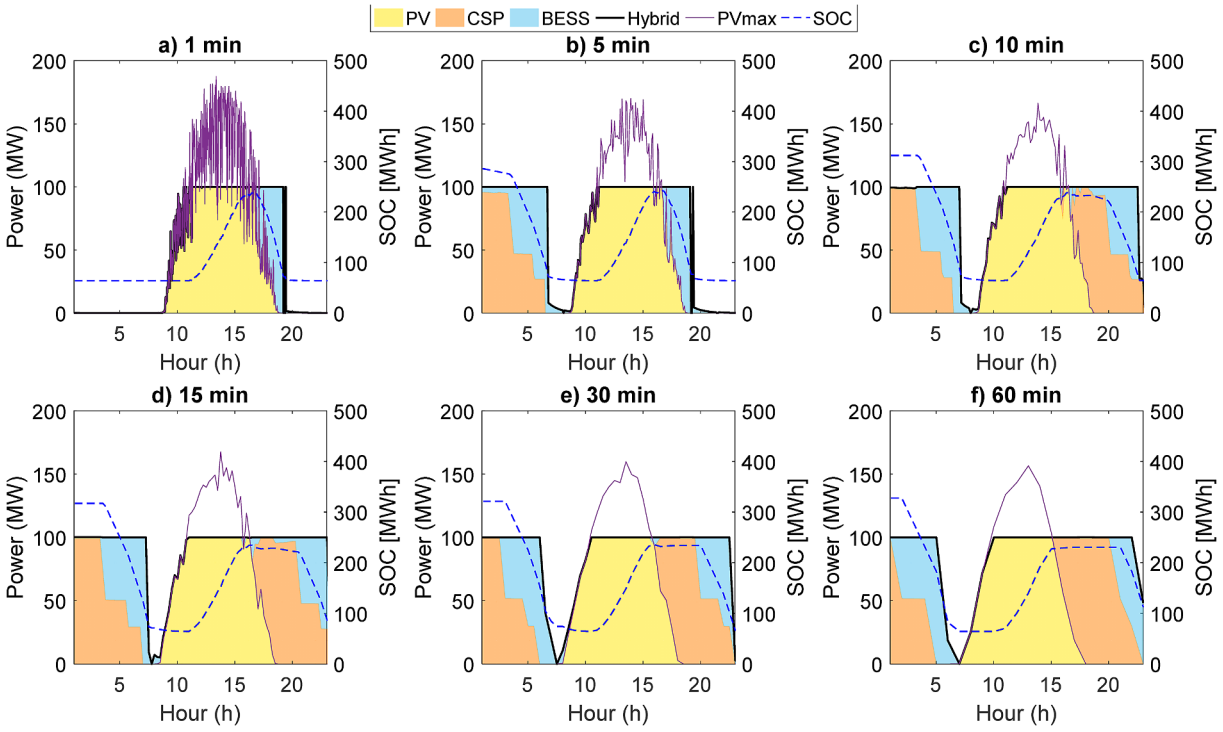

Fig. 6. Production profile of the hybrid plant at Carrera Pinto in a variable day (July 21st) for different time steps: a) 1 min, b) 5 min, c) 10 min, d) 15 min, e) 30 min, and f) 60 min.

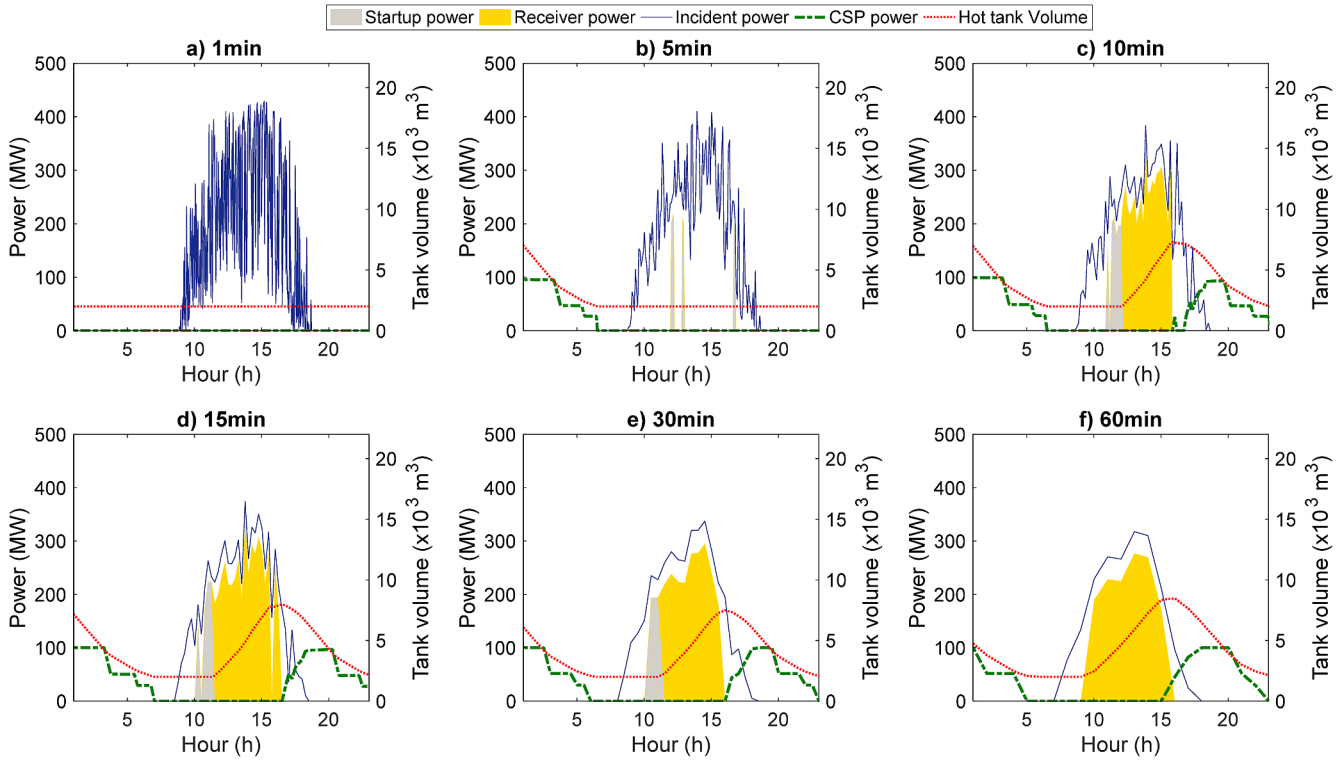

Fig. 7. Central receiver operation during a variable day (July 21st) in Carrera Pinto for different time steps: a) 1 min, b) 5 min, c) 10 min, d) 15 min, e) 30 min, and f) 60 min.

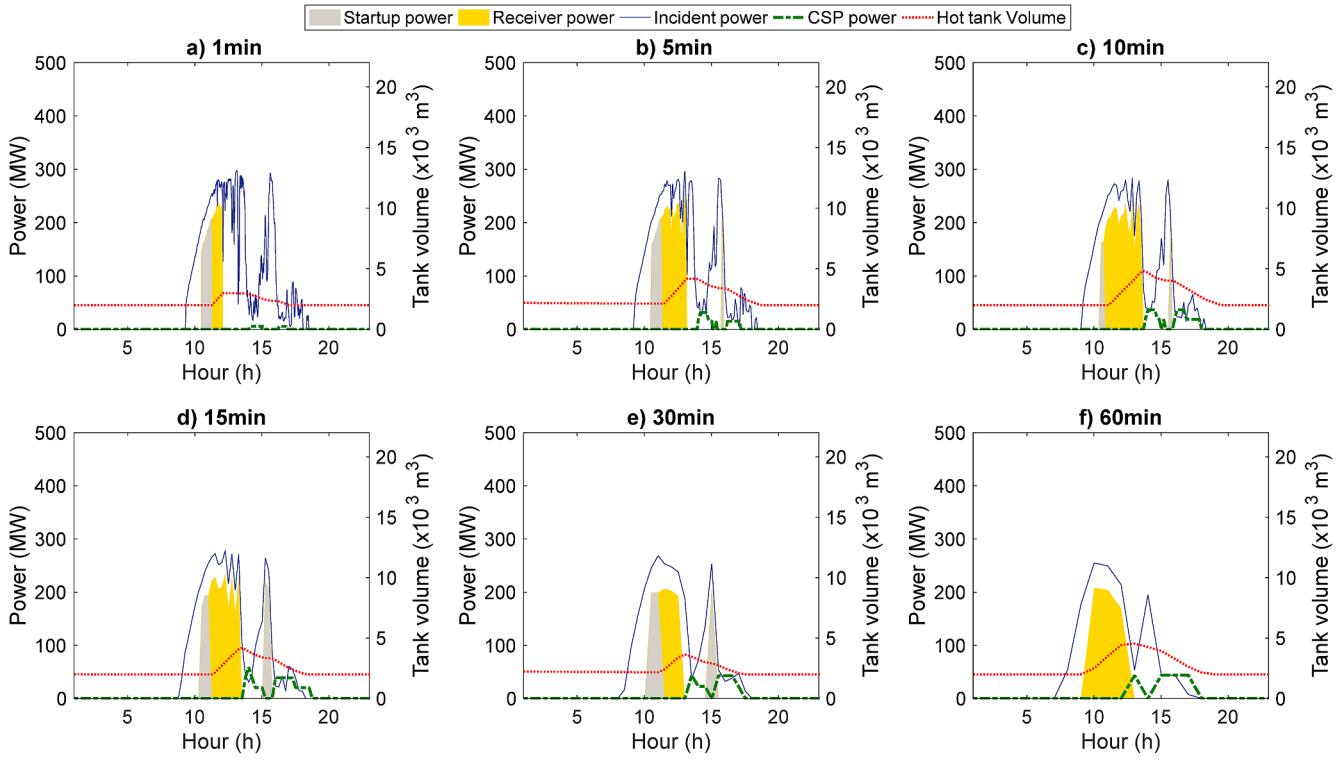

Fig. 8. Central receiver operation during a variable day (June 19th) in Santiago for different time steps: a) 1 min, b) 5 min, c) 10 min, d) 15 min, e) 30 min, and f) 60 min.

the start-up, ramp-up, ramp-down, and shut-down procedures, which led to affecting the operation time and the energy produced by the receiver. This situation directly impacts the volume of molten salts that is charged to the hot tank, and therefore, the operation time of the CSP plant. Control procedures represent a restriction to satisfy minimum operational requirements, which in reality are implemented in solar thermal power plants to guarantee safe operating conditions and to avoid damages in the receiver and the power block components.

Table 7
Annual total generation and percentage differences using different time steps for Carrera Pinto.

	Annual generation (MWh)					Percentage Difference with respect to 1 min results (%)				
Time step (min)	PV	CSP	BESS	Hybrid	Receiver	PV	CSP	BESS	Hybrid	Receiver
1	314,937	392,856	49,053	756,846	1,006,437	–	–	–	–	–
5	315,528	418,052	46,342	779,923	1,070,744	0.19%	6.41%	−5.53%	3.05%	6.39%
10	315,354	430,588	43,916	789,857	1,100,696	0.13%	9.60%	−10.47%	4.36%	9.37%
15	315,169	435,367	43,479	794,015	1,114,718	0.07%	10.82%	−11.36%	4.91%	10.76%
30	313,525	437,433	43,663	794,621	1,117,010	−0.45%	11.35%	−10.99%	4.99%	10.99%
60	309,584	449,675	41,611	800,870	1,150,053	−1.70%	14.46%	−15.17%	5.82%	14.27%

Table 8
Annual total generation and percentage differences using different time steps for Santiago.

	Annual generation (MWh)					Percentage Difference with respect to 1 min results (%)				
Time step (min)	PV	CSP	BESS	Hybrid	Receiver	PV	CSP	BESS	Hybrid	Receiver
1	259,723	263,320	37,342	560,384	687,657	–	–	–	–	–
5	260,412	279,210	35,352	574,973	730,170	0.27%	6.03%	−5.33%	2.60%	6.18%
10	260,634	285,496	34,278	580,408	744,829	0.35%	8.42%	−8.21%	3.57%	8.31%
15	260,993	291,056	32,870	584,919	760,939	0.49%	10.53%	−11.98%	4.38%	10.66%
30	260,339	290,194	33,464	583,997	757,135	0.24%	10.21%	−10.38%	4.21%	10.10%
60	257,950	304,486	31,283	593,719	796,892	−0.68%	15.63%	−16.22%	5.95%	15.88%

However, results indicate that control operation parameters were more realistically captured with time resolutions of 1 min and 5 min, while with higher time steps, information regarding the variability of the DNI is so reduced that operational curves of the hybrid plant changed dramatically.

5.2. Annual performance prediction

The yearly performance of the hybrid plant for different time resolution is evaluated in this section. Table 7 and Table 8 present the total yearly generation of each component of the hybrid plant for both locations (Carrera Pinto and Santiago) using different time steps and the percentage differences with respect to the 1-minute results. In this case, the PV column represents the net energy produced by the PV power plant applying the curtailment of the baseload demand ($100MW_e$). In general, it was observed that the PV generation presents minimal variations as the time resolution is lower with a maximum decrease of −1.70% and −0.68% with the 60-minute data in Carrera Pinto and Santiago, respectively; and the percentage differences were below ± 0.50% with the rest of the time steps.

In contrast, the most significant differences occurred in the CSP and BESS generation in both locations. First, it was obtained that the CSP total generation tends to increase as the time step is larger, which is caused by a higher prediction of the energy delivered by the receiver that presented variations up to 14.27% and 15.88% with the 60-minute data in Carrera Pinto and Santiago, respectively. As it was mentioned before, these differences are related to the operation time prediction of the receiver that changes as the time resolution is varied. Notably, the DNI profile changes as the time resolution is lower, which has an impact on the start-up procedures and operation time of the receiver during the day. This also affects the volume and temperature of the molten salts tanks used to operate the CSP plant during the non-sunlight hours.

Furthermore, the BESS contribution to the annual hybrid plant generation decreased in both locations as the time step increases due to the solar irradiance variability is highly reduced. This causes a rise in the CSP generation and a reduction in the energy required of the battery bank to complement the PV production during the day. In the case of Carrera Pinto, a maximum percentage difference on the BESS generation of −15.17% was found with the 60-minute data, while in Santiago was about −16.22%. Regarding the total annual generation of the hybrid plant, the maximum percentage difference found in Carrera Pinto was 5.82% with the 60-minute data. In contrast, a maximum difference of 5.95% was obtained in Santiago. These results indicate a similar tendency of overestimating the annual generation of the hybrid plant as the time resolution is decreased in both locations, with approximately the same percentage differences, even though Santiago is a location that presents a more unfavorable solar resource than Carrera Pinto. that the annual total hybrid generation is higher as the time resolution of the solar irradiance data and the simulation is lower in both locations, which indicates an overestimation of the hybrid plant production when larger time steps are used.

5.3. Techno-economic results

This section presents the results of the techno-economic analysis performed for different cases of study. In first instance, results of the base case, which considered the same configuration of hybrid plant for two locations, are presented through a comparative analysis of the capacity factor and the LCOE varying the time step. Secondly, three more cases of study were included to analyze the impact of time resolution for different plant configurations and dispatch strategies.

5.3.1. Base case results

Table 9 and Table 10 present the techno-economic results of the simulations performed as base case in this study. Results are in terms of the capacity factor and LCOE calculated for the different time steps in both locations, and the percentage differences with respect 1-minute results. In general, capacity factors between 82 and 86% were obtained in Carrera Pinto, and LCOEs between 85 and 81 USD/MWh, while in Santiago the capacity factors were lower as it was expected, within a range between 60 and 64%, and with higher LCOES between 119 and 112 USD/MWh. Regardless of the location, the LCOE decreases as the time resolution is lower, mainly due to the overestimation of the hybrid plant's annual generation when the time step is increased.

Table 9 and Table 10 also report the simulation time of each time step normalized with respect to the simulation time using the 1-minute time resolution. It is observed that as the time step is increased, the simulation time drops significantly. For instance, only for the simulation using a 5-minute time step, the simulation is about 76.5% faster than with the 1-minute time step, while with the 60-minute time

Table 9
Techno-economic results for the hybrid plant in Carrera Pinto for different time steps.

Time step (min)	CF (%)	LCOE (USD/MWh)	Hybrid plant generation (MWh)	Normalized Simulation Time (-)	%Diff CF	%Diff LCOE
1	82.08	85.98	756,846	1.000	–	–
5	84.58	83.55	779,923	0.229	3.05%	−2.82%
10	85.66	82.56	789,857	0.128	4.36%	−3.98%
15	86.11	82.15	794,015	0.083	4.91%	−4.46%
30	86.17	82.10	794,621	0.050	4.99%	−4.52%
60	86.85	81.51	800,870	0.023	5.82%	−5.20%

Table 10
Techno-economic results for the hybrid plant in Santiago for different time steps.

Time step (min)	CF (%)	LCOE (USD/MWh)	Hybrid plant generation (MWh)	Normalized Simulation Time (-)	%Diff CF	%Diff LCOE
1	60.77	119.29	560,384.28	1.000	–	–
5	62.35	116.37	574,973.27	0.235	2.60%	−2.45%
10	62.94	115.32	580,407.75	0.115	3.57%	−3.33%
15	63.43	114.46	584,919.06	0.090	4.38%	−4.05%
30	63.33	114.63	583,997.16	0.040	4.21%	−3.91%
60	64.39	112.84	593,718.84	0.025	5.95%	−5.41%

resolution, the simulation duration is decreased a 97.5%. These results are similar in both locations. This reduction in the simulation time is important when fast simulation models are needed; however, the compression of data also leads to a loss of information of the variability, which causes an overestimation in the energy production.

In the case of Carrera Pinto, percentage differences in the capacity factor and LCOE were around ± 3% with the 5-minute time resolution, between ± 4–5% for time steps between 10 and 30 min, and the most significant variation was obtained performing hourly simulations between ± 5–6%. Furthermore, Table 10 shows similar percentage differences for the capacity factor and LCOE in Santiago. In this case, percentage differences were between ± 2–3% using the 5-minute resolution, ± 3–4% for the 10–30 min time steps, and between ± 5–6% with the 60-minute time resolution.

It is important to take into account that differences between 2 and 6% in the annual generation of a hybrid plant may be considered small; however, they can be decisive at the time of getting funding through PPA or winning a bid. For instance, in the case of Chile, energy projects must compete between them to offer the lowest cost of electricity in energy blocks, and even small differences in the offers can lead to different results.

5.3.2. Comparison of cases of study

To diversify results and findings of the methodology raised in this paper, four study cases are presented in this subsection to compare the influence of the time resolution impact on the modeling of different plant configurations and dispatch strategies. Table 11 shows the description of the configurations considered for this comparative analysis. In first instance, it is included the base case configuration previously simulated in Carrera Pinto, which presents an oversized PV field with a medium CSP plant size (Base Case CP). The second case of study (Hybrid CD) represents a similar configuration of the Cerro Dominador (CD) plant, currently being developed in northern Chile, which has a 100 MW PV plant, and a molten solar tower with an approximate SM of 3 and 17.5 h of TES. This configuration represents an undersized PV with respect to the CSP, and it was added a battery bank of 100 MWh. The third case of study represents only the CSP part of the CD plant to compare the time resolution impact in a standalone CSP plant (CSP CD), and the last configuration (Hybrid 150 peak) presents the same configuration as the base case but with a peak strategy in which the demand increases to 150 MW_e during peak hours (05:00–09:00, 18:00–21:00), and the rest of the day the plant must generate 100 MW_e. Furthermore, all the cases of study in this section were modeled only in Carrera Pinto.

Table 11
Description of cases of study.

Case of study	Location	Demand (MW)	PV size (MW)	SM (-)	TES capacity (h)	BESS size (MWh)	PV Tracking (-)
Base Case CP	CP	100	190	2	14	400	0
Hybrid CD	CP	100	100	3	17.5	100	1
CSP CD	CP	100	–	3	17.5	–	–
Hybrid 150 peak	CP	150 MW (05:00–09:00, 18:00–21:00) 100 MW for the rest	190	2	14	400	0

Table 12
Results for different case studies varying the time resolution of the simulation.

Study case	Time Resolution	1	5	10	15	30	60
Base Case CP	CSP generation [MWh]	392,856	418,052	430,588	435,367	437,433	449,675
	Hybrid generation [MWh]	756,846	779,923	789,857	794,015	794,621	800,870
	LCOE [USD/MWh]	85.98	83.55	82.56	82.15	82.10	81.51
Hybrid CD	CSP generation [MWh]	468,768	502,457	515,824	521,864	523,806	535,879
	Hybrid generation [MWh]	746,469	777,364	789,226	794,642	794,270	805,272
	LCOE [USD/MWh]	91.84	88.36	87.09	86.53	86.57	85.45
CSP CD	CSP generation [MWh]	598,543	638,526	656,619	666,307	663,094	685,173
	Hybrid generation [MWh]	–	–	–	–	–	–
	LCOE [USD/MWh]	100.56	94.51	92.02	90.74	91.16	88.35
Hybrid 150 peak	CSP generation [MWh]	406,969	433,389	445,681	451,625	451,401	463,241
	Hybrid generation [MWh]	821,982	848,642	860,814	866,488	865,439	874,183
	LCOE [USD/MWh]	79.37	76.99	75.96	75.49	75.58	74.87

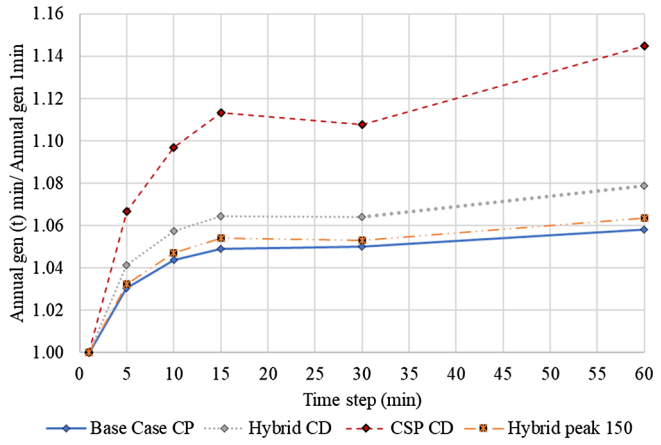

Fig. 9. Normalized annual generation vs. time step of the simulation for different cases.

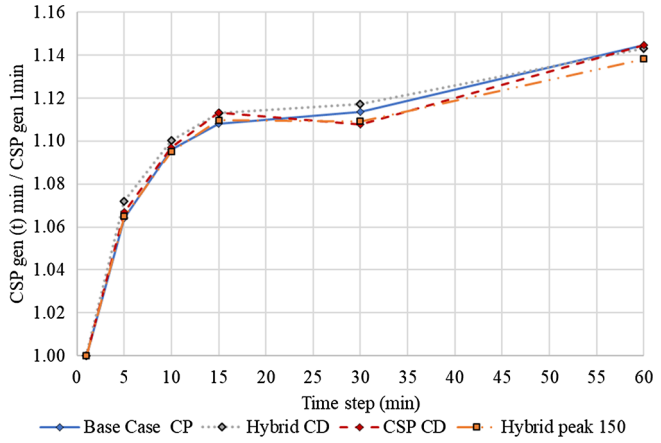

Fig. 10. Normalized CSP generation vs. time step of the simulation for different cases.

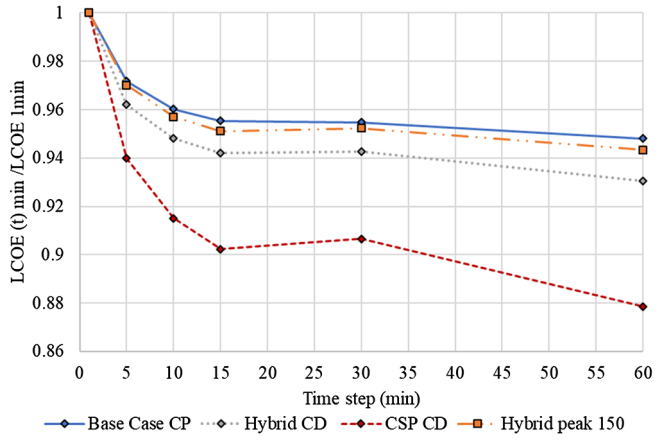

Fig. 11. Normalized LCOE vs. time step of the simulation for different cases.

Simulations varying the time step and the meteorological data were performed to obtain the annual results and techno-economic indicators of every case. Results of these simulations are presented in detail in Table 12, showing the annual production of only the CSP plant ($E_{CSP(t)}$), the annual hybrid total generation of the plant ($E_{hybrid(t)}$), and the LCOE ($LCOE_{(t)}$). Then, these three values were normalized with respect to the results found with the 1-minute time resolution ($E_{hybrid(t=1min)}$, $E_{CSP(t=1min)}$, $LCOE_{(t=1min)}$, respectively), to be analyzed and compared, as Eq. (6)–(8) indicate. Variables with the "*n*" superscript would represent the normalized values.

$$E^{n}_{hybrid(t)} = \frac{E_{hybrid(t)}}{E_{hybrid(t=1min)}} \tag{6}$$

$$E^{n}_{CSP(t)} = \frac{E_{CSP(t)}}{E_{CSP(t=1min)}} \tag{7}$$

$$LCOE^{n}_{(t)} = \frac{LCOE_{(t)}}{LCOE_{(t=1min)}} \tag{8}$$

In this manner, Fig. 9, Fig. 10, and Fig. 11 present the comparison of the normalized variables for every case at different time steps. Regarding the normalized annual generation ($E^{n}_{hybrid(t)}$), Fig. 9 illustrates how the components sizing and the plant configuration influence the time resolution impact. First, results indicate that the most substantial differences in the estimated annual production occur with the standalone CSP plant (CSP-CD). In this case, variations around 7% with respect to the 1-minute results occur even by using the 5-minute time resolution, and differences up to 14% are accounted when the 60-minute time resolution is implemented. In comparison, the cases with a hybrid plant scheme present a lower impact of the time resolution in the annual production, with a maximum difference of 8% obtained with the 60-minute data in the Hybrid-CD case.

In the case of the hybrid plants, it is also observed that the components sizing influences the impact of time resolution on the performance prediction of the system. For instance, both cases with a large and oversized PV system with regards to the CSP (Base case CP and Hybrid 150 peak) obtained the smallest normalized differences as the time step was increased, within a range of 3–6% depending on the time resolution, while the case with an undersized PV plant and a large CSP system (Hybrid CD) was more affected by the temporal resolution than the other two cases for, with differences between 4 and 8% in the annual production. It is also worth to mention that in the case of Hybrid peak 150, the dispatch strategy at peak hours did not cause any significant in the influence of time resolution since it obtained similar results to the base case. This result shows that varying the sizing of the components of a hybrid plant has a higher impact than modifying the dispatch strategy in the evaluation of the time resolution.

Regarding the normalized CSP generation ($E^{n}_{CSP(t)}$), Fig. 10 shows that when only the CSP generation is considered (in the case of a hybrid plant it would be represented by the annual contribution of the CSP-TES plant to the total production, and in the standalone CSP plant it would be the net yearly generation), the impact of time resolution is within the same range of variation regardless the configuration of the plant, which means, the production of a CSP plant is affected in the same way by the time resolution either if it is evaluated in a hybrid scheme or a standalone system. Nevertheless, Figs. 8 and 9 show that differences in the total annual generation are smaller than the variations accounted for only the CSP generation, which indicates that the CSP plant is the system most influenced by the time resolution.

Results also indicate that the sizing of the PV field with respect to the CSP plant plays an important role in the impact that time resolution has on the performance of a hybrid plant. Since the PV plant has the priority dispatch on the hybrid plant, it can produce around 40–50% of the total annual generation. Besides this, the yearly PV plant production is barely affected by the time resolution, which it helps to attenuate the significant impact that time resolution has on the estimation of the CSP

production. Therefore, the effect of time resolution in the performance prediction on a hybrid plant is lower when configurations with an oversized PV system with respect to the CSP plant are considered, while the effect is higher when the CSP plant is oversized with regards to the PV system.

Finally, Fig. 11 shows the variation in the normalized LCOE ($LCOE^{n}_{(t)}$) for every time step and case. Since the annual generation is overestimated as the time resolution is decreased, the opposite trend is evidenced in the LCOE. This can also be observed in Table 12. In this way, $LCOE^{n}_{(t)}$ is underestimated with respect to the 1-minute result at every case, with the largest difference obtained for the standalone CSP plant using the 60-minute data. This result is in concordance with the tendencies obtained in Fig. 9. It was also obtained that time resolution impact on the $LCOE^{n}_{(t)}$ is smaller for the hybrid plant cases, showing the effect that the components sizing and their costs have on the final impact of time resolution on the LCOE estimation.

6. Discussion

In this work, it is analyzed the operation, performance, and dispatchability of a hybrid CSP-PV plant integrated with a TES and battery bank under different conditions of time resolution. In this section, the main considerations implemented to perform this work, and some discussions regarding the results obtained in the study are explained and developed below:

- The operating mode and the sizing of the components can lead to different outcomes of the time resolution impact on the performance of the hybrid plant. In this study, the operating mode of the hybrid plant prioritizes the PV output, and it dispatches the CSP plant around the PV, while the BESS is used as a back-up to soft PV variations and to complement the CSP output. However, the analysis showed in Section 5.3.2 indicates that the effect of having an oversized or undersized PV plant with respect to the CSP, it only affects the magnitude of the overestimation of the annual generation, but the tendency with respect to the time step remains the same. Moreover, different dispatch strategies such as baseload and a peak demand were considered between the cases of study, and results showed that the impact of time resolution was more influenced by the sizing of the components than the profile demand.
- Solar data in 1-min resolution implemented in this work comes from ground measurements performed by a sensor located at only one point. This data presents a very high level of DNI variability, which may lead to an underestimation of the incident power on the solar field, since the DNI variability may be attenuated if a larger area is considered. The DNI variability has a significant impact on the control operation of the receiver, and consequently, the CSP performance. Therefore, a more representative data could be obtained if 1-minute data coming from several measuring points (between 2 and 4) located within the plant area (1–2 km distance) is averaged, which may capture the actual variability that affects the whole solar field area. Moreover, the 1-minute based data was used as a reference to compare the results of different time resolutions due to the lack of data coming from a real power plant. Nevertheless, the best way to determine the most appropriate time resolution to simulate the plant would be to compare real data with the results obtained for every time step and then, stablishing which time step captures the actual behavior of the operating facility. However, due to the lack of CSP projects operating worldwide, results of this study indicate that the 5-minute based data could be the most appropriate time step to capture the actual variability occurring in the whole area of the plant.
- Ground-measured solar and meteorological data of 1-minute has the drawback that is representative of only one particular year. Conversely, a Typical Meteorological Year (TMY) condenses multi-year long-term time series into one representative year, which is created from satellite-based models with a temporal resolution of 30 min or 1 h that leads to an inevitable loss of the DNI variability information. In this manner, discussion regarding if minute-based measurements are better than using the available hourly TMY data does not have yet a final answer, basically because the use of ground-measurements or TMYs would be influenced by a relationship between the desired precision and the limitations of processing time. For instance, a good practice in the industry is to perform simulations with a TMY and start running a measurement campaign at the site of interest in parallel with the project development. Later, simulations with sub-hourly data shall be performed to determine a more realistic performance of the plant. Moreover, an interesting research topic could be related to how the hourly TMY data can be adapted to sub-hourly based data to capture the transient effects, as well as assessing how to translate the DNI variability in terms of uncertainty to the hourly data to improve a TMY that could lead to similar results than the 1-minute based data.
- The development of a hybrid CSP-PV project comprises different phases (preliminary feasibility evaluation, bankability assessment, real technical-operation simulations, or bid preparation) that present different requirements of the energy models' accuracy. Results obtained in this work have shown the importance of considering the influence of time resolution on energy simulations; therefore, some advantages and drawbacks of using a specific time resolution are discussed. For pre-feasibility evaluations, 1-hour can be the most appropriate time resolution since it provides the fastest simulation time, which is needed to run techno-economic design optimizations that involve a significant number of simulations and to show the potential of different locations; however, the outcomes would lead to an overestimation of the CSP performance, thus, they would be very optimistic. In the development phase, additional simulations using sub-hourly timesteps between 1 and 5 min can represent an advantage since they allow to capture the variability effects on energy production. In this way, models with a high time resolution can reduce the uncertainty on the estimation of the plant generation lowering the risk perception from the financing entities, even though simulations will require a longer computational time. Finally, in a bid preparation for electric tenders, simulations with a high time resolution would lead to a conservative approach guaranteeing a minimum energy target. In contrast, if the computational time is a concern, 10–15 min timesteps can be implemented to capture the variability effects partially and to set higher energy targets, nevertheless, this approach can be risky if these targets cannot be accomplished at the time of operating the plant.

7. Conclusions

The impact of time resolution on the modeling of a hybrid solar power plant was carried out considering a central-receiver power plant coupled with a two-tank molten salt TES, a PV plant, and a battery bank. The operation and performance of the hybrid plant were evaluated, varying the time resolution of the simulation from 1, 5, 10, 15, 30 to 60 min. The hybrid plant was modeled in two locations of Chile for the base case, and different configurations and dispatch strategies were evaluated as cases of study. The daily performance of the hybrid plant, the total annual generation, the capacity factor, and the LCOE were also assessed. Main conclusions which provide the summarized findings of this work are presented as it follows:

- Daily operation analysis showed that the performance of thermal systems such as the receiver and the power block of the CSP plant was the most affected by the time resolution variation, followed by the BESS, while the effect on the daily PV generation was negligible.
- Variation in the receiver operation with the time resolution was a result of the application of operation controls, including start-up, ramp-up, ramp-down, and shut-down procedures that affect the operation time and the energy produced by the receiver. These control procedures of the receiver and power block were more realistically captured with time steps between 1 and 5 min, while with higher time steps, information regarding the DNI variability was lost.
- In general, the annual generation of the hybrid plant was overestimated as the time step was increased. The maximum percentage differences in the total yearly hybrid production with respect to the 1-minute results were obtained with the hourly data, reaching 5.83% and 5.95% in Carrera Pinto and Santiago, respectively. Moreover, the largest variations were obtained in the annual CSP generation with 14.27% and 15.88% in both locations, respectively. Regarding the techno-economic results, percentage differences in the capacity factor and LCOE were around ± 2–3% in both sites using the 5-minute time resolution, while higher differences between ± 4–6% were found for time steps between 10 and 60 min. In this way, differences about 2–6% may be small, but they can be decisive at the time of evaluating projects to obtain financing or long-term contracts energy contracts in tenders.
- The tendency of overestimation as the time step is increased was also found in the cases of study in which the sizing of the components and the dispatch strategy were varied. In this way, results showed that the impact of time resolution on the performance estimation of a standalone CSP plant is much more significant than in a hybrid plant. Moreover, the effect of the time step was lower for oversized PV configurations with respect to the CSP, and variations were higher when the CSP plant is oversized with regards to the PV system.
- Results of this work indicate that the 5-minute time resolution can be the most appropriate time step to use in the modeling of a hybrid plant since it provides a well-balanced relationship between accuracy and computational time of the simulation; however, authors want to emphasize that the use of temporal resolution will mainly depend on the purpose of the simulation, how much accuracy is expected from the results, and the computational time limitations. In this way, the advantages and drawbacks of implementing different time steps at every phase of the development of a large-scale solar power plant project were discussed and presented in this study.

Declaration of Competing Interest

The authors declare that they have no known competing financial interests or personal relationships that could have appeared to influence the work reported in this paper.

Acknowledgements

Authors gratefully acknowledge the financial support of the Pontificia Universidad Católica de Chile VRI doctoral scholarship and the support from Fraunhofer Chile Research –Center of Solar Energy Technologies by the Corfo project 13CEI2-21803. Authors also appreciate the support from CONICYT/FONDAP 15110019 “Solar Energy Research Center“- SERC-Chile, A. Zurita would like to acknowledge the funding from CONICYT PFCHA/Doctorado Nacional 2019 - 21191591, and C. Mata-Torres the funding from CONICYT PFCHA/Doctorado Nacional 2018 - 21181537.

Appendix A. Supplementary Data

Supplementary data represents the coefficients of the power block regression model described in the following equations:

$$W_{net} = a_1 \cdot T_{amb} + a_2 \cdot T_{inHTF} + a_3 \cdot T_{inHTF} \cdot T_{amb} + a_4 \cdot \dot{m}_{inHTF} + a_5 \cdot \dot{m}_{inHTF} \cdot T_{amb} + a_6 \cdot \dot{m}_{inHTF} \cdot T_{inHTF} + a_7 + a_8 \cdot \dot{m}_{inHTF}^{\,2} + a_9 \cdot T_{inHTF}^2 + a_{10} \cdot T_{amb}^2 \quad \text{(A1)}$$

$$\dot{m}_{cond} = b_1 \cdot T_{amb} + b_2 \cdot T_{inHTF} + b_3 \cdot T_{inHTF} \cdot T_{amb} + b_4 \cdot \dot{m}_{inHTF} + b_5 \cdot \dot{m}_{inHTF} \cdot T_{amb} + b_6 \cdot \dot{m}_{inHTF} \cdot T_{inHTF} + b_7 + b_8 \cdot \dot{m}_{inHTF}^{2} + b_9 \cdot T_{inHTF}^2 + b_{10} \cdot T_{amb}^2 \quad \text{(A2)}$$

$$T_{outHTF} = c_1 \cdot T_{amb} + c_2 \cdot T_{inHTF} + c_3 \cdot T_{inHTF} * T_{amb} + c_4 \cdot \dot{m}_{inHTF} + c_5 \cdot \dot{m}_{inHTF} \cdot T_{amb} + c_6 \cdot \dot{m}_{inHTF} \cdot T_{inHTF} + c_7 + c_8 \cdot \dot{m}_{inHTF}^{2} + c_9 \cdot T_{inHTF}^2 + c_{10} \cdot T_{amb}^2 \quad \text{(A3)}$$

Appendix B. Cost Data

See Tables B1 and B2.

Table B1
Economic parameters considered for the CSP plant.

Description	Unit	Value
Direct capital cost		
Heliostat field	USD/m^2	160
Power block	USD/kW$_e$	1100
Storage	USD/kWh$_t$	29
Tower cost	USD/m	95,000
Receiver cost	USD/kW$_t$	140
Contingency and other costs	-	10%
Indirect capital cost		
EPC profit rate	% of direct cost	10%
Sales tax	%	0
Operation and Maintenance		
Fixed cost by capacity	USD/kW-yr	48
Variable cost by generation	USD/MWh	3.7

Table B2
Economic parameters considered for the PV plant and BESS.

Description	Unit	Value
PV plant		
Direct capital cost		
Module cost	USD/W_{dc}	0.30
Inverter cost	USD/W_{ac}	0.05
Electrical BoS	USD/W_{dc}	0.08
Mechanical BoS	USD/W_{dc}	0.09
Installation labor	USD/W_{dc}	0.10
Installer margin and overhead	USD/W_{dc}	0.05
Contingency	%	3
Indirect capital cost		
EPC profit rate	USD/W_{dc}	0.08
Sales tax	%	0
O&M costs		
O&M cost for fixed-tilt	USD/kW-yr	9
BESS		
Capital cost		
Cost of storage section	USD/kWh	209
Power conversion system cost	USD/kW	70
Structural BoS	USD/kW	10
Electrical BoS	USD/kW	70
Operation and Maintenance		
Fixed O&M cost	USD/kW-yr	6.9
Variable O&M cost	USD/MWh	2.1
Replacement		
Replacement cost	USD/kWh	2/3 of the cost of storage section

Appendix C. Cost Structure

$$Af = \frac{r}{1 - \frac{1}{(1+r)^L}} \tag{C.1}$$

$$C_{inv,hybrid} = C_{inv,PV} + C_{inv,CSP} + C_{inv,BESS} \tag{C.2}$$

$$C_{O\&M,hybrid} = C_{O\&M,PV} + C_{O\&M,CSP} + C_{O\&M,BESS} \tag{C.3}$$

$$C_{inv,PV} = C_{d,PV} + C_{id,PV} \tag{C.4}$$

$$C_{d,PV} = [(c_{mod} + c_{BoS,PV} + c_{inst} + c_{overh})P_{PV}^{DC} + c_{invs} \bullet P_{invs}^{AC}](1 + \%Cont_{PV}) \tag{C.5}$$

$$C_{id,PV} = C_{d,PV} \bullet \%EPC_{PV} \tag{C.6}$$

$$C_{O\&MPV} = c_{O\&M,PV} \bullet P_{PV}^{AC} \tag{C.7}$$

$$C_{inv,CSP} = C_{d,CSP} + C_{id,CSP} \tag{C.8}$$

$$C_{d,CSP} = [C_{HF} + C_{pb} + C_{TES} + C_{tow} + C_{rec} + C_{other}](1 + \%Cont_{CSP}) \tag{C.9}$$

$$C_{HF} = c_{HF} A_{HF} \tag{C.10}$$

$$C_{pb} = c_{pb} P_{gross,turb}^{e} \tag{C.11}$$

$$C_{TES} = c_{TES} P_{TES}^{th} \tag{C.12}$$

$$C_{tow} = c_{tow} \bullet (h_{tow} - h_{rec}) \tag{C.13}$$

$$C_{rec} = c_{rec} P_{rec}^{th} \tag{C.14}$$

$$C_{id,CSP,t} = C_{d,CSP} \bullet \%EPC_{CSP} \tag{C.15}$$

$$C_{CO\&M,CSP} = c_{f,O\&M,CSP} \bullet P_{net,CSP}^{e} + c_{v,O\&M,CSP} \bullet E_{CSP} \tag{C.16}$$

$$C_{inv,PV} = (c_{PCS,BESS} + c_{BoS,BESS})P_{BESS}^{e} + c_{stor} \bullet S_{BESS} \tag{C.17}$$

$$C_{O\&M,BESS} = c_{f,O\&M,BESS} \bullet P_{BESS}^{e} + c_{v,O\&M,BESS} \bullet E_{disch,BESS} \tag{C.18}$$

$$z = E_{disch,BESS}/S_{BESS} \tag{C.19}$$

$$t = n/z \tag{C.20}$$

$$C_{rep,BESS} = \sum_{j=1}^{k} \frac{1}{(1+r)^{jt}} c_{rep} \bullet S_{BESS} \tag{C.21}$$

Appendix D. Supplementary data

Supplementary data to this article can be found online at https://doi.org/10.1016/j.solener.2020.03.100.

References

ABB, 2017. ULTRA-750/1100/1500 (North America) [WWW Document]. accessed 1.1.18. http://new.abb.com/power-converters-inverters/solar/central/ultra/750kw-1100kw-1500kw.

Aly, A., Bernardos, A., Fernandez-Peruchena, C.M., Solvang Jensen, S., Pedersen, A.B., 2019. Is Concentrated Solar Power (CSP) a feasible option for Sub-Saharan Africa?: Investigating the techno-economic feasibility of CSP in Tanzania. Renew. Energy 135, 1224–1240. https://doi.org/10.1016/j.renene.2018.09.065.

Ayala-Gilardón, A., Sidrach-de-Cardona, M., Mora-López, L., 2018. Influence of time resolution in the estimation of self-consumption and self-sufficiency of photovoltaic facilities. Appl. Energy 229, 990–997. https://doi.org/10.1016/j.apenergy.2018.08.072.

Boretti, A., 2018. Cost and production of solar thermal and solar photovoltaics power plants in the United States. Renew. Energy Focus 26, 93–99. https://doi.org/10.1016/j.ref.2018.07.002.

Bravo, R., Friedrich, D., 2018. Two-stage optimisation of hybrid solar power plants. Sol. Energy 164, 187–199. https://doi.org/10.1016/j.solener.2018.01.078.

Cocco, D., Migliari, L., Petrollese, M., 2016. A hybrid CSP-CPV system for improving the dispatchability of solar power plants. Energy Convers. Manag. 114, 312–323. https://doi.org/10.1016/j.enconman.2016.02.015.

Dieckmann, S., Dersch, J., Giuliano, S., Puppe, M., Lüpfert, E., Hennecke, K., Pitz-Paal, R., Taylor, M., Ralon, P., 2017. LCOE reduction potential of parabolic trough and solar tower. In: CSP technology until 2025, in: AIP Conference Proceedings, pp. 160004. https://doi.org/10.1063/1.4984538.

Escobar, R.A., Cortés, C., Pino, A., Salgado, M., Pereira, E.B., Martins, F.R., Boland, J., Cardemil, J.M., 2015. Estimating the potential for solar energy utilization in Chile by satellite-derived data and ground station measurements. Sol. Energy 121, 139–151. https://doi.org/10.1016/j.solener.2015.08.034.

Fu, R., Feldman, D., Margolis, R., 2018a. U. S. Solar Photovoltaic System Cost Benchmark : Q1 2018, NREL. https://doi.org/10.7799/1325002.

Fu, R., Remo, T., Margolis, R., Fu, R., Remo, T., Margolis, R., 2018. 2018. S. Utility-Scale Photovoltaics- Plus-Energy Storage System Costs Benchmark. U.

Green, A., Diep, C., Dunn, R., Dent, J., 2015. High Capacity Factor CSP-PV Hybrid Systems. Energy Procedia 69, 2049–2059. https://doi.org/10.1016/j.egypro.2015.03.218.

Guédez, R., Spelling, J., Laumert, B., Fransson, T., 2014. Optimization of Thermal Energy Storage Integration Strategies for Peak Power Production by Concentrating Solar Power Plants. Energy Procedia 49, 1642–1651. https://doi.org/10.1016/j.egypro.2014.03.173.

Hamilton, William T., Husted, Mark A., Newman, Alexandra M., Braun, Robert J., Wagner, Michael J., 2020. Dispatch optimization of concentrating solar power with utility-scale photovoltaics. Optim Eng 21 (1), 335–369. https://doi.org/10.1007/s11081-019-09449-y.

Hirsch, T., Dersch, J., Fluri, T., Garcia-Barberena, J., Giuliano, S., Hustig-Diethlem, F., Meyer, R., Schmidt, N., Seitz, M., Yildiz, E., 2017. SolarPACES guideline for bankable STE yield assessment, IEA-SolarPACES.

IRENA, 2018. Renewable Power Generation Costs in 2017. International Renewable Energy Agency. https://doi.org/10.1007/SpringerReference_7300.

IRENA, 2012. Renewable Energy Technologies: Cost Analysis Series Concentrating Solar Power, Comprehensive Renewable Energy. Abu Dhabi. https://doi.org/10.1016/B978-0-08-087872-0.00319-X.

Jorgenson, J., Mehos, M., Denholm, P., 2016. Comparing the net cost of CSP-TES to PV deployed with battery storage. In: in: AIP Conference Proceedings, pp. 080003. https://doi.org/10.1063/1.4949183.

Kassem, A., Al-Haddad, K., Komljenovic, D., 2017. Concentrated solar thermal power in Saudi Arabia: Definition and simulation of alternative scenarios. Renew. Sustain. Energy Rev. 80, 75–91. https://doi.org/10.1016/j.rser.2017.05.157.

Mata-Torres, C., Zurita, A., Cardemil, J.M., Escobar, R.A., 2019. Exergy cost and thermoeconomic analysis of a Rankine Cycle + Multi-Effect Distillation plant considering time-varying conditions. Energy Convers. Manag. 192, 114–132. https://doi.org/10.1016/j.enconman.2019.04.023.

Meybodi, M.A., Beath, A.C., 2016. Impact of cost uncertainties and solar data variations on the economics of central receiver solar power plants: An Australian case study. Renew. Energy 93, 510–524. https://doi.org/10.1016/j.renene.2016.03.016.

NREL, 2018. Solar Power tower Integrated Layout and Optimization Tool [WWW Document]. accessed 1.15.19. https://www.nrel.gov/csp/solarpilot.html.

Pan, C.A., Dinter, F., 2017. Combination of PV and central receiver CSP plants for base load power generation in South Africa. Sol. Energy 146, 379–388. https://doi.org/10.1016/j.solener.2017.02.052.

Paravalos, C., Koutroulis, E., Samoladas, V., Kerekes, T., Sera, D., Teodorescu, R., 2014. Optimal design of photovoltaic systems using high time-resolution meteorological data. IEEE Trans. Ind. Informatics 10, 2270–2279. https://doi.org/10.1109/TII.2014.2322814.

Patnode, A.M., 2006. Simulation and performance evaluation of parabolic trough solar power plants. Univ. Wisconsin-Madison Master 5–271.

Petrollese, M., Cocco, D., 2016. Optimal design of a hybrid CSP-PV plant for achieving the full dispatchability of solar energy power plants. Sol. Energy 137, 477–489. https://doi.org/10.1016/j.solener.2016.08.027.

PV Info Link, 2018. Spot prices [WWW Document]. accessed 4.9.19. https://en.pvinfolink.com/.

REN21, 2019. 2019 Global Status Report [WWW Document]. URL hthttps://www.ren21.net/wp-content/uploads/2019/05/gsr_2019_full_report_en.pdf (accessed 2.2.20).

Rojas, R.G., Alvarado, N., Boland, J., Escobar, R., Castillejo-Cuberos, A., 2019. Diffuse fraction estimation using the BRL model and relationship of predictors under Chilean, Costa Rican and Australian climatic conditions. Renew. Energy 136, 1091–1106. https://doi.org/10.1016/j.renene.2018.09.079.

Schwarzbözl, P., Eiden, U., Pitz-Paal, R., Zentrum, D., Scott, J., 2006. A TRNSYS Model Library for Solar Thermal Electric Components (STEC) Reference Manual. DLR, Germany.

Sharma, C., Sharma, A.K., Mullick, S.C., Kandpal, T.C., 2017. Cost reduction potential of parabolic trough based concentrating solar power plants in India. Sundaray and Kandpal IRENA. https://doi.org/10.1016/j.esd.2017.10.003.

Starke, A.R., Cardemil, J.M., Escobar, R., Colle, S., 2018. Multi-objective optimization of hybrid CSP-PV system using genetic algorithm. Energy. https://doi.org/10.1016/j.energy.2017.12.116.

Starke, A.R., Cardemil, J.M., Escobar, R.A., Colle, S., 2016. Assessing the performance of hybrid CSP + PV plants in northern Chile. Sol. Energy 138, 88–97. https://doi.org/10.1016/j.solener.2016.09.006.

SunEdison, 2015. MEMC Silvantis M330 Module [WWW Document]. URL http://fmscopk.com/wp-content/uploads/2015/08/SunEdison.pdf (accessed 1.1.18).

Valenzuela, C., Mata-Torres, C., Cardemil, J.M., Escobar, R.A., 2017. CSP + PV hybrid solar plants for power and water cogeneration in northern Chile. Sol. Energy 157, 713–726. https://doi.org/10.1016/j.solener.2017.08.081.

Wagner, M.J., 2008. Simulation and Predictive Performance Modeling of Utility-Scale Central Receiver System Power Plants. University of Wisconsin-Madison.

Zakeri, B., Syri, S., 2015. Electrical energy storage systems: A comparative life cycle cost analysis. Renew. Sustain. Energy Rev. 42, 569–596. https://doi.org/10.1016/j.rser.2014.10.011.

Zhai, R., Chen, Y., Liu, H., Wu, H., Yang, Y., Hamdan, M.O., 2018. Optimal Design Method of a Hybrid CSP-PV Plant Based on Genetic Algorithm Considering the Operation Strategy. Int. J. Photoenergy 2018. https://doi.org/10.1155/2018/8380276.

Zurita, A., Mata-Torres, C., Valenzuela, C., Felbol, C., Cardemil, J.M., Guzmán, A.M., Escobar, R.A., 2018. Techno-Economic Evaluation of a Hybrid CSP-PV Plant Integrated with Thermal Energy Storage and a Large-Scale Battery Energy Storage System for Base Generation. Sol. Energy 173, 1262–1277. https://doi.org/10.1016/j.solener.2018.08.061.